Influence of Wind on Subtidal Salt Intrusion and Stratification in Well-Mixed and Partially Stratified Estuaries

Jongbloed, Hendrik; Schuttelaars, Henk M.; Dijkstra, Yoeri M.; Donkers, Paul B.; Hoitink, Antonius J.F.

Important note
To cite this publication, please use the final published version (if applicable).
Please check the document version above.

Influence of Wind on Subtidal Salt Intrusion and Stratification in Well-Mixed and Partially Stratified Estuaries

HENDRIK JONGBLOED,[a] HENK M. SCHUTTELAARS,[b] YOERI M. DIJKSTRA,[b] PAUL B. DONKERS,[b] AND ANTONIUS J. F. HOITINK[a]

[a] *Hydrology and Quantitative Water Management Group, Wageningen University and Research, Wageningen, Netherlands*
[b] *Delft Institute of Applied Mathematics, Delft University of Technology, Delft, Netherlands*

ABSTRACT: An idealized width-averaged model is employed to study the influence of wind stress on subtidal salt intrusion and stratification in well-mixed and partially stratified estuaries. We show that even in mild conditions, wind forcing can influence the estuarine salinity structure in a substantial way. By studying the role of wind forcing on dominant salt transport balances and associated salt transport regimes, we unify and clarify ambiguous observations from previous authors regarding the influence of wind stress: the response of the estuarine salinity structure to wind forcing is different depending on the underlying dominant salt transport balance, which in turn was found to determine whether wind-induced salinity shear, wind-induced modulation of the longitudinal salt distribution, or wind-induced mixing dominates.

SIGNIFICANCE STATEMENT: The purpose of this idealized study is to better understand how wind influences the salinity distribution in estuaries on large time scales. This is important because a change in winds can move saline water further inland, threatening freshwater availability and the natural balance of delicate ecosystems. We clarify the sometimes ambiguous observations regarding the influence of wind on the salt distribution and highlight the importance of including average wind forcing in analyses of estuarine dynamics on large time scales.

KEYWORDS: Estuaries; Baroclinic flows; Dispersion; Wind stress; Idealized models

1. Introduction

Salt intrusion and stratification in estuaries depend on various physical forcings, including river discharge, tides, and wind. There is ample evidence that even in relatively mild conditions, wind forcing can be as important as riverine and tidal forcing in governing the estuarine salinity structure and dominant salt transport balances (see, e.g., Weisberg and Sturges 1976). The response of salt intrusion and stratification to wind forcing has been documented in many field and complex model studies, with salt intrusion responding fairly consistently, but stratification being reported to respond ambiguously.

Field studies of North et al. (2004) and Uncles and Stephens (2011) and a complex model study of Xu et al. (2008) indicate that salt intrusion increases for down-estuary (seaward) winds and decreases for up-estuary (landward) winds. Down-estuary wind enhances estuarine circulation, pushing near-bed salinity further inland. Up-estuary wind tends to increase the along-channel salinity gradient (North et al. 2004) by decreasing salinity shear or even reversing the net direction of estuarine circulation (Xie and Li 2018; Lange and Burchard 2019), resulting in reduced salt intrusion.

The response of stratification to wind forcing shows greater variability. Various field and model studies have reported on an increase in stratification for down-estuary winds and a decrease for up-estuary winds (Wang 1979; Weisberg and Sturges 1976; Elliott 1978; van de Kreeke and Robaczewska 1989; North et al. 2004; Scully et al. 2005; Xie and Li 2018). Conversely, in field studies by Goodrich et al. (1987) and Stanley and Nixon (1992), an overall decrease in stratification for both down- and up-estuary winds has been observed. Then, Geyer (1997) and Lai et al. (2018) have documented an increase in stratification for up-estuary winds and a decrease for down-estuary winds, in a field and complex model study, respectively.

Various hypotheses have been put forward to explain these considerable differences in estuarine response to wind forcing. First, Chen and Sanford (2009) considered a case where up-estuary winds decreased stratification, whereas down-estuary winds could both decrease and increase stratification, depending on the wind stress magnitude. This ambiguous response of stratification to wind forcing was explained to be a result of the competition between wind straining of the salinity field and wind-induced mixing of the upper layer. For up-estuary winds, both straining and wind-induced mixing reduce stratification. For low down-estuary wind speeds, wind straining of the salinity field increases stratification, whereas for high wind speeds, wind-induced turbulence dominates, making the system more well mixed and thus reducing stratification. Second, two-dimensional hypotheses involving the longitudinal salt distribution have been proposed by various authors. Geyer (1997) and Scully et al. (2005) focused on the effect of wind on the along-channel salinity gradient, which to a large degree correlates with density stratification. For down-estuary winds, they reported a decrease of along-channel salinity

gradient, and vice versa for up-estuary winds. As argued by Burchard (2009), the sensitivity of stratification to wind-induced along-channel salinity gradient modulation is often greater than its sensitivity to wind-induced mixing.

From the above, it follows that there is no unified understanding of the sensitivity of salt intrusion and stratification to wind that simultaneously incorporates the three mechanisms proposed previously: the combined effects of wind on shear, mixing and the along-channel salinity distribution. In view of this, the present research aims to provide a physical explanation of the observed sensitivity of salt intrusion and stratification to wind, by revealing dominant transport balances across a wide range of river discharge, tidal, and wind stress magnitudes. To achieve this, we use the subtidal, width-averaged model by Ralston et al. (2008), which is an adaptation with wind of the model of MacCready (2004) that was first proposed by Hansen and Rattray (1965). We propose a new, analytical model solution method and we derive precise boundaries in parameter space, demarcating the regions of model assumption (in)validity. Furthermore, by inspecting underlying transport balances, we use this model to analytically identify four salt transport regimes in parameter space and investigate the sensitivity of salt intrusion and stratification within each model regime.

The remainder of this paper is organized as follows. In section 2, we show that the dynamics of the model depend on just three dimensionless numbers: a Froude number, representing river discharge; an estuarine Rayleigh number, representing mixing and hence tidal forcing; and a dimensionless wind stress number. In section 3, these numbers are used to classify idealized estuaries on the basis of salt transport regimes. We will analyze the specific characteristics of these regimes with a focus on the behavior of salt intrusion and stratification within each regime. Results from existing literature will be discussed in section 4 with the aim of explaining different observations by previous authors on the basis of our newly found dominant salt transport regimes. The main findings are summarized in section 5.

2. Model development

a. Model equations

The subtidal flow and salinity dynamics of estuaries are governed by the tidally averaged conservation of momentum, mass, and salinity. Following MacCready (2004) and Ralston et al. (2008), these equations are linearized and width averaged. We consider an idealized rectangular estuary with constant depth H, constant width B, and infinite length. Focusing on equilibria, the subtidal flow and salinity of well-mixed to partially mixed estuaries are described by

$$(K_M u_z)_z = g\zeta_x - g\beta_h s_x z, \tag{1}$$

$$u_x + w_z = 0, \tag{2}$$

$$(us)_x + (ws)_z = (K_H s_x)_x + (K_S s_z)_z, \tag{3}$$

in the domain $x < 0$, $-H < z < 0$, using the rigid lid approximation. Symbols x and z represent the longitudinal and vertical coordinates, respectively, and $u(x, z)$ and $w(x, z)$ are corresponding flow velocity components. The salinity field is denoted by $s(x, z)$. Subscript notation involving x or z represents partial differentiation. The acceleration of gravity, haline contraction coefficient, and longitudinal surface gradient are denoted by g, β_h, and ζ_x, respectively. In the rigid lid approximation, $g\zeta_x$ must be interpreted as an imposed longitudinal pressure gradient, rather than an actual surface gradient. The term K_M denotes the effective vertical eddy viscosity, assumed constant and uniform throughout the estuary. Last, K_H and K_S denote horizontal and vertical eddy diffusivity coefficients, both also assumed constant and uniform throughout the estuary, where K_H parameterizes tidal dispersion of salt. Flow and salinity are required to satisfy the following boundary conditions:

$$K_M u_z = \frac{\tau_w}{\rho_0} \quad \text{at} \quad z = 0, \tag{4}$$

$$K_M u_z = \frac{\tau_b}{\rho_0} \quad \text{at} \quad z = -H, \tag{5}$$

$$w = 0 \quad \text{at} \quad z = 0 \text{ and } z = -H, \tag{6}$$

$$\int_{-H}^{0} u \, dz = \frac{Q}{B} \quad \text{for} \quad x \to -\infty, \tag{7}$$

$$K_S s_z = 0 \quad \text{at} \quad z = 0 \quad \text{and} \quad z = -H, \tag{8}$$

$$s = s_0 \quad \text{at} \quad (x, z) = (0, -H), \tag{9}$$

$$s = 0 \quad \text{for} \quad x \to -\infty. \tag{10}$$

Wind stress and bottom friction enter the model via surface and bottom boundary conditions, according to Eqs. (4) and (5). In these equations, ρ_0 is the density of freshwater and τ_w denotes the surface wind stress, proportional to the square of the relative wind speed at a height of 10 m above the water surface u_a (Wu 1969):

$$\tau_w = C_d \rho_a u_a^2 \text{sign}(u_a), \tag{11}$$

where C_d is an air–water drag coefficient and ρ_a is the density of air. The wind stress τ_w is assumed constant and uniform in space. In Eq. (5), the bottom stress is linearized as (see, e.g., Zimmerman 1982):

$$\tau_b = s_f \rho_0 u. \tag{12}$$

This partial slip boundary condition generalizes the no-slip boundary condition employed by MacCready (2004), which is recovered by letting $s_f \to \infty$. The partial slip parameter in the above expression is given by

$$s_f = a\frac{K_M}{H}, \tag{13}$$

with $a = 2$, which approximately captures the relation between the eddy viscosity and bed friction in a barotropic uniform flow using a k–ϵ model (Dijkstra et al. 2017). The third and fourth boundary conditions, given in Eq. (6), are kinematic boundary conditions that ensure the free surface and estuarine bottom are impermeable. River discharge is incorporated by means of Eq. (7). Equation (8) prevents salt from diffusing into the estuarine bottom or through the free surface. The seaward and landward salinity boundary conditions, Eqs. (9) and (10), require the bottom seaward salinity to equal the oceanic salinity s_0 and riverine runoff to have zero salinity. By virtue of our solution method, these boundary conditions are sufficient to obtain a unique model solution.

All model parameters are taken constant and uniform throughout the model domain and should be interpreted as typical values, parametrically taking into account lateral, longitudinal, and intratidal variations. Moreover, the choice of constant and uniform parameters allows us to work with a limited parameter set in order to investigate model sensitivity w.r.t. a wide range of possible parameter configurations. In section 4, implications for model applicability are discussed.

b. Equation development

1) DIMENSIONAL MODEL SOLUTION

Following MacCready (2004), we solve for the flow velocity u and salinity field s by decomposing the physical quantities in depth-averaged and depth varying parts:

$$u(x, z) = \overline{u}(x) + u'(x, z), \tag{14}$$

$$s(x, z) = \overline{s}(x) + s'(x, z), \tag{15}$$

where depth-averaged salinity is defined by

$$\overline{s}(x) = \frac{1}{H} \int_{-H}^{0} s(x, z)\, dz, \tag{16}$$

and $\overline{u}(x)$ is defined in the same way. Accordingly, $\overline{(\cdot')} = (\overline{\cdot})' = 0$.

We employ the approximation based on Pritchard (1952), who argued that for well-mixed and partially stratified estuaries it holds that

$$s'_x \ll \overline{s}_x \tag{17}$$

for all (x, z), where s'_x denotes the vertically varying part of the longitudinal salinity gradient. The full salinity field in the baroclinic term in the momentum equation Eq. (1) is then replaced by its depth average, yielding

$$(K_M u_z)_z = g\zeta_x - g\beta_h \overline{s}_x z. \tag{18}$$

Below, we first solve for the flow $\overline{u}$, u', and w. Next, we consider the depth-varying salinity s'. At this point, u' and s' still depend on the unknown depth-averaged salinity gradient $\overline{s}_x$. Finally, a nonlinear differential equation for the depth-averaged salinity $\overline{s}$ will be derived and solved to yield the model

solution (u, s). Below, details of the solution procedure are given.

(i) Flow

Three forcings may be distinguished for the flow: river runoff, density differences, and surface wind stress. River runoff induces both a depth-averaged flow contribution, denoted by $\overline{u}_F$ (flushing) and a shear flow, denoted by $u_{R'}$. Density differences induce gravitational circulation, a shear flow denoted by $u_{G'}$, and wind induces a shear flow denoted by $u_{W'}$. Since the governing momentum Eq. (18) and the boundary conditions (4) and (7) are linear in u, the governing equations can be solved for the individual forcing contributions separately. Their sum yields the complete solution for $u(x, z)$.

From mass conservation, Eq. (2), and the upstream boundary condition, Eq. (7) and the assumption of constant and uniform H and B, it follows that the depth-averaged flow $\overline{u}$ is constant and uniform throughout the estuary. It reads

$$\overline{u}(x) = \underbrace{\overline{u}}_{\overline{u}_F} = \frac{Q}{BH}. \tag{19}$$

To obtain an expression for the shear flow u', Eq. (18) is solved separately for each forcing by applying the appropriate boundary conditions. Adding all contributions yields the following expression for the flow (see also Hansen and Rattray 1965):

$$u'(x, z) = \underbrace{\overline{u} P_1\!\left(\frac{z}{H}\right)}_{u'_R} + \underbrace{\frac{g\beta_h H^3}{K_M} \overline{s}_x(x) P_2\!\left(\frac{z}{H}\right)}_{u'_G} + \underbrace{\frac{\tau_w H}{\rho_0 K_M} P_3\!\left(\frac{z}{H}\right)}_{u'_W}. \tag{20}$$

Note that the density-driven contribution u'_G depends on the (still unknown) depth-averaged salinity gradient $\overline{s}_x(x)$. The vertical profiles of velocity shear P_1, P_2, and P_3 are similar to the well-known Hansen and Rattray (1965) shape functions (see also MacCready 2004; Geyer 1997; Ralston et al. 2008), but differ slightly because of the partial slip bottom boundary condition. They are provided in appendix A.

For completeness, the vertical flow velocity is obtained by solving Eqs. (2) and (6) for w. One obtains

$$w(x, z) = -\frac{g\beta_h H^4}{K_M} \overline{s}_{xx}(x) P_7\!\left(\frac{z}{H}\right). \tag{21}$$

(ii) Salinity shear

Depth-averaging the salt conservation Eq. (3) gives

$$(\overline{u}\,\overline{s})_x + (\overline{u's'})_x = K_H \overline{s}_{xx}, \tag{22}$$

where boundary conditions (6) and (8) were used. Subtracting the depth-averaged salt conservation equation (22) from the full Eq. (3), one obtains

$$\overline{u}s_x' + u_x'\overline{s} + u'\overline{s}_x + (u's')'_x + w_z\overline{s} + w_z s' + ws_z' = K_H s_{xx}' + K_S s_{zz}'.$$
(23)

Assumption Eq. (17) may be employed to derive a dominant balance in Eq. (23). Following MacCready (2004), only two terms are assumed to be of leading order:

$$u'\overline{s}_x = K_S s_{zz}'.$$
(24)

Adopting the above dominant balance restricts the dynamics of the model to well-mixed and partially stratified conditions. Substitution of the flow shear equation (20) in Eq. (24) leads to an expression for the salinity shear s' in terms of the depth-averaged salinity $\overline{s}$. Employing the linearity of Eq. (24), the salinity shear is given by

$$s'(x,z) = \underbrace{\frac{H^2}{K_S}\overline{u}\overline{s}_x(x)P_4\left(\frac{z}{H}\right)}_{s_R'} + \underbrace{\frac{g\beta_h H^5}{K_S K_M}\overline{s}_x^2(x)P_5\left(\frac{z}{H}\right)}_{s_G'}$$
$$+ \underbrace{\frac{\tau_w H^3}{\rho_0 K_S K_M}\overline{s}_x(x)P_6\left(\frac{z}{H}\right)}_{s_W'}.$$
(25)

Again, the salinity shear shape functions P_4, P_5, and P_6 are similar to the ones provided by Hansen and Rattray (1965).

(iii) Depth-averaged salinity

An equation for $\overline{s}(x)$ follows from integrating the salt balance, Eq. (3), over the estuarine cross section. The cross-sectionally averaged salt transport through the estuary cross section is equal to the sum of the advective transport us and transport related to the tidal dispersion, parameterized by $-K_H s_x$. Since our model is in equilibrium, and by using the fact that riverine runoff has no salinity, see Eq. (9), the total, cross-sectionally and tidally averaged transport of salt equals zero:

$$0 = \frac{1}{H}\int_{-H}^{0}(us - K_H s_x)dz$$
$$= \overline{u}\,\overline{s} - K_H\overline{s}_x$$
$$= -\overline{u}\,\overline{s} - \overline{u's'} + K_H\overline{s}_x,$$
(26)

which is identical to Eq. (12) of MacCready (2004) and the longitudinally integrated depth-averaged salt balance (22). Substituting Eqs. (20) and (25) in Eq. (26) yields the following equation for $\overline{s}(x)$:

$$\underbrace{C_1\frac{g^2\beta_h^2 H^8}{K_S K_M^2}\overline{s}_x^3(x)}_{t_{GG}} + \underbrace{C_2\frac{\overline{u}g\beta_h H^5}{K_S K_M}\overline{s}_x^2(x)}_{t_{GR}} + \underbrace{C_3\frac{\tau_w g\beta_h H^6}{K_S K_M^2 \rho_0}\overline{s}_x^2(x)}_{t_{GW}}$$
$$+ \underbrace{C_4\frac{\overline{u}^2 H^2}{K_S}\overline{s}_x(x)}_{t_{RR}} + \underbrace{C_5\frac{\overline{u}\tau_w H^3}{\rho_0 K_S K_M}\overline{s}_x(x)}_{t_{RW}} + \underbrace{C_6\frac{\tau_w^2 H^4}{\rho_0^2 K_S K_M^2}\overline{s}_x(x)}_{t_{WW}}$$
$$+ \underbrace{K_H\overline{s}_x(x)}_{t_D} - \underbrace{\overline{u}\,\overline{s}(x)}_{t_F} = 0.$$
(27)

Riverine flushing transport t_F is the depth-averaged salinity export due to river runoff. Transport resulting from cross

correlations between runoff shear, density differences, and wind are denoted by the subscripts R, G, and W. These cross correlations arise from the product $\overline{u's'}$ in Eq. (26), written out as the depth average of $(u_R' + u_G' + u_W')(s_R' + s_G' + s_W')$. Last, the transport of salt due to tidal dispersion is denoted by t_D. The constants $C_1, \ldots, C_6$ are known coefficients and can be found in appendix A.

2) DIMENSIONLESS MODEL SOLUTION

The dimensional equations and solutions derived above can be cast in dimensionless form by introducing $\sigma = z/H$, $c = \sqrt{g\beta_h s_0 H}$, $X = xc/K_H$, $U = u/c$, and $\Sigma = s/s_0$. Next, the vertical eddy diffusivity K_s is related to the vertical eddy viscosity K_M using a constant and uniform Prandtl–Schmidt number, having a value taken from Ralston et al. (2008):

$$K_S = K_M/\text{Sc}, \text{ with Sc} = 2.2.$$
(28)

The resulting dimensionless flow field reads

$$U(X,\sigma) = \underbrace{\text{Fr}}_{\overline{U}_F} + \underbrace{\text{Fr}P_1(\sigma)}_{U_R'} + \underbrace{\text{Ra}\overline{\Sigma}_X(X)P_2(\sigma)}_{U_G'} + \underbrace{\text{Fw}P_3(\sigma)}_{U_W'},$$
(29)

and the dimensionless salinity is given by

$$\Sigma(X,\sigma) = \overline{\Sigma}(X) + \underbrace{\text{RaFr}\overline{\Sigma}_X(X)P_4(\sigma)}_{\Sigma_{R'}} + \underbrace{\text{Ra}^2\overline{\Sigma}_X^2(X)P_5(\sigma)}_{\Sigma_{G'}}$$
$$+ \underbrace{\text{RaFw}\overline{\Sigma}_X(X)P_6(\sigma)}_{\Sigma_{W'}}.$$
(30)

These expressions depend on three dimensionless numbers:

$$\text{Fr} = \frac{Q}{cBH} \quad \text{(Froude number)},$$
(31)

$$\text{Ra} = \frac{c^2 H^2}{K_M K_H} \quad \text{(estuarine Rayleigh number)},$$
(32)

$$\text{Fw} = \frac{1}{c}\frac{\tau_w H}{\rho_0 K_M} \quad \text{(wind straining number)}.$$
(33)

The estuarine Froude number Fr (see, e.g., Geyer and MacCready 2014; Dijkstra and Schuttelaars 2021), the estuarine Rayleigh number Ra (Hansen and Rattray 1965), and the wind strain number Fw (Ralston et al. 2008) fully determine the model solution, since the bottom friction parameter a and the Prandtl–Schmidt number Sc are kept constant in this study. The dimensionless equivalent of the transport balance Eq. (27), with dimensionless transports denoted by capital letters, is given by

$$\underbrace{\Lambda_{GG}^3\overline{\Sigma}_X^3}_{T_{GG}} + \underbrace{\Lambda_{GR}^2\overline{\Sigma}_X^2}_{T_{GR}} + \underbrace{\Lambda_{GW}^2\overline{\Sigma}_X^2}_{T_{GW}} + \underbrace{\Lambda_{RR}\overline{\Sigma}_X}_{T_{RR}}$$
$$+ \underbrace{\Lambda_{RW}\overline{\Sigma}_X}_{T_{RW}} + \underbrace{\Lambda_{WW}\overline{\Sigma}_X}_{T_{WW}} + \underbrace{\Lambda_D\overline{\Sigma}_X}_{T_D} - \underbrace{\Lambda_F\overline{\Sigma}_X}_{T_F} = 0.$$
(34)

Scale	Definition	Approximate
Λ_{GG}^3	$C_1 \text{Ra}^3$	$0.000\,11\text{Ra}^3$
Λ_{GR}^2	$C_2 \text{Ra}^2 \text{Fr}$	$0.0017\text{Ra}^2\text{Fr}$
Λ_{GW}^2	$C_3 \text{Ra}^2 \text{Fw}$	$0.0011\text{Ra}^2\text{Fw}$
Λ_{RR}	$C_4 \text{Ra} \text{Fr}^2$	$0.0067\text{Ra}\,\text{Fr}^2$
Λ_{RW}	$C_5 \text{Ra}\,\text{Fr}\,\text{Fw}$	$0.0086\text{Ra}\,\text{Fr}\,\text{Fw}$
Λ_{WW}	$C_6 \text{Ra}\,\text{Fw}^2$	$0.0030\text{Ra}\,\text{Fw}^2$
Λ_D	1	1
Λ_F	Fr	Fr

Equation (34) is the main transport balance of the present dimensionless model. Within this balance, different dominant balances may exist, depending on the governing dimensionless numbers (Fr, Ra, Fw). The dimensionless scales Λ in Eq. (34) are defined in Table 1 and can be interpreted as (powers of) length scales relative to the dispersive length scale $L_D = K_H/c$, determining the relative importance of transport processes.

The dominant transport balances that may be formed within Eq. (34) will be discussed in section 3.

3) SOLVING FOR THE DEPTH-AVERAGED SALINITY

In the previous paragraph, the dimensionless transport balance, Eq. (34) was derived, which is a nonlinear differential equation for the depth-averaged salinity. This section provides details on the solution method of Eq. (34). For readability, the equation is rewritten as

$$\alpha \overline{\Sigma}_X^3 + \beta \overline{\Sigma}_X^2 + \gamma \overline{\Sigma}_X - \delta \overline{\Sigma} = 0, \tag{35}$$

where

$$\begin{aligned} \alpha &= \Lambda_{GG}^3, \\ \beta &= \Lambda_{GR}^2 + \Lambda_{GW}^2, \\ \gamma &= \Lambda_{RR} + \Lambda_{RW} + \Lambda_{WW} + \Lambda_D, \\ \delta &= \Lambda_F. \end{aligned} \tag{36}$$

(i) Seaward boundary condition

To solve Eq. (35) for $\overline{\Sigma}$, one boundary condition is required for the depth-averaged dimensionless salinity. This boundary condition follows from the requirement that $\Sigma(0, -1) = 1$, see Eq. (9). Substituting this condition in Eq. (30) yields

$$1 = \overline{\Sigma}(0) + \text{Ra}\overline{\Sigma}_X(0)[\text{Fr}P_4(-1) + \text{Ra}\overline{\Sigma}_X(0)P_5(-1) + \text{Fw}P_6(-1)]. \tag{37}$$

Using Eq. (37) to express $\overline{\Sigma}_0 = \overline{\Sigma}(0)$ in terms of $\overline{\Sigma}_{X0} = \overline{\Sigma}_X(0)$ and substituting the resulting expression in Eq. (35) at $X = 0$, a cubic equation for $\overline{\Sigma}_{X0}$ is found:

$$\alpha \overline{\Sigma}_{X0}^3 + \beta_0 \overline{\Sigma}_{X0}^2 + \gamma_0 \overline{\Sigma}_{X0} - \delta = 0, \tag{38}$$

with

$$\begin{aligned} \beta_0 &= \beta + \delta \text{Ra}^2 P_5(-1), \\ \gamma_0 &= \gamma + \delta \text{Ra}[\text{Fr}P_4(-1) + \text{Fw}P_6(-1)], \end{aligned} \tag{39}$$

which can be solved analytically to find $\overline{\Sigma}_{X0}$. From this, $\overline{\Sigma}_0$ can be computed by substitution in Eq. (35).

(ii) Up-estuary salinity computation

To solve for the up-estuary depth-averaged salinity, we employ a new fully analytical solution procedure, rather than the numerical integration approach employed in MacCready (2004). This solution method assumes constant and uniform parameter values across the model domain. Both the depth-averaged salinity $\overline{\Sigma}$ and the distance from the seaward boundary X are obtained as a function of a parameter $r \leq 0$, with $r = 0$ the parameter value at the seaward boundary $X = 0$:

$$\overline{\Sigma}(r) = \delta^{-1}(\alpha \overline{\Sigma}_{X0}^3 e^{3r} + \beta \overline{\Sigma}_{X0}^2 e^{2r} + \gamma \overline{\Sigma}_{X0} e^r), \tag{40}$$

$$X(r) = \delta^{-1}\left[\frac{3}{2}\alpha \overline{\Sigma}_{X0}^2(e^{2r} - 1) + 2\beta \overline{\Sigma}_{X0}(e^r - 1) + \gamma r\right]. \tag{41}$$

Similarly, an expression for the depth-averaged salinity gradient in terms of r is obtained:

$$\overline{\Sigma}_X(r) = \overline{\Sigma}_{X0} e^r. \tag{42}$$

The above parametric solution is derived in more detail in appendix B.

(iii) Salt intrusion

One of the main advantages of the analytical solution (40), (41) is that the salt intrusion length can be computed without integrating Eq. (35). We define the dimensionless salt intrusion length Λ_s as the dimensionless distance between the seaward side of the estuary and the location where the depth-averaged salinity equals 1 psu:

$$\Lambda_s = |X(r = r_s)|, \tag{43}$$

$$\text{with } r_s = [r \leq 0 : \overline{\Sigma}(r) = 1/30]. \tag{44}$$

Substitution of Eqs. (35) and (40) in Eq. (44) yields an equation for $\exp(r_s)$:

$$\alpha \overline{\Sigma}_{X0}^2 \exp(3r_s) + \beta \overline{\Sigma}_{X0} \exp(2r_s) + \gamma e^r = 1/30, \tag{45}$$

from which r_s can be explicitly computed by analytically solving the cubic equation in $\exp(r_s)$. Using the obtained expression for r_s, Λ_s can be obtained using Eq. (43).

(iv) Seaward stratification

Having computed the seaward salinity gradient $\overline{\Sigma}_{X0}$, one can straightforwardly compute the seaward stratification Φ_0 as the difference between the bottom and surface salinity at $X = 0$:

$$\begin{aligned} \Phi_0 &:= 1 - \Sigma(0, 0) \\ &= 1 - \overline{\Sigma}_0 + \text{Ra}\overline{\Sigma}_{X0}(C_7\text{Fr} + C_8\text{Ra}\overline{\Sigma}_{X0} + C_9\text{Fw}), \end{aligned} \tag{46}$$

where the positive constants C_7, C_8, and C_9 are given by $-P_4(0)$, $-P_5(0)$, and $-P_6(0)$, respectively (numerical values are provided in appendix A). For stably stratified estuaries, the seaward stratification satisfies $\Phi_0 \in [0, 1]$, where smaller values represent well-mixed systems and larger values more stratified systems.

4) MODEL APPLICABILITY AND LIMITATIONS

The elegance and straightforward solution procedure of the present model is made possible by a number of restricting model assumptions. These restrictions cause three types of possible model behavior that are considered invalid.

1) No unique real model solution exists. This can be the case when solving for $\overline{\Sigma}_{X0}$, Eq. (38), or when solving for the salt intrusion length, Eq. (45), or for the up-estuary model solution, Eqs. (40) and (41). This behavior of nonuniqueness correlates with large values of Fr and Ra, for which advective momentum terms may not be neglected, the Pritchard (1952) assumption becomes less accurate, and certain up-estuary wind numbers.

2) The salinity distribution becomes negative. This behavior is again encountered for large values of Fr and Ra, for which numbers the model assumptions become questionable.

3) Unstable stratification is encountered, that is, the salinity distribution is not monotonously decreasing for increasing $\sigma \in [-1, 0]$. This behavior is exclusively encountered for strong enough up-estuary winds (Fw < 0), depending also on Fr and Ra.

Analytical solutions to determine when these model limitations arise, are provided in appendix B.

3. Results

To identify the influence of subtidal wind stress on salt intrusion and stratification, a sensitivity study was conducted for a large range of values for Fr, Ra, and Fw. Within this three-dimensional parameter space, it is found that this sensitivity can be captured by just four different dominant balances [in Eq. (34)]. These are the only possible dominant balances of the present model and each constitute a model regime. The first two regimes were already described by Chatwin (1976) and Dijkstra and Schuttelaars (2021) and identified as dispersive and Chatwin regimes. The inclusion of wind forcing results in two additional regimes. In section 3a, all four regimes will be discussed, with an emphasis on the two new regimes, which will be illustrated using two typical examples. In section 3b, we identify the regions in parameter space spanned by Fr, Ra, and Fw where the different dominant balances occur. The behavior of salt intrusion, stratification and their connection with the along-channel salinity gradient will be related to the four regimes in section 3.

a. Four salt transport regimes

1) REGIME I AND II: DISPERSIVE AND CHATWIN

To facilitate future discussion, a short summary of the dispersive and Chatwin regimes is given here. These were already identified by Hansen and Rattray (1965), Chatwin (1976), MacCready (2004), and Dijkstra and Schuttelaars (2021). Regime I, the dispersive regime, is characterized by a dominant balance between river-induced flushing T_F and tidally dispersive import T_D of salt. Hence, the dominant salt balance (34) in Regime I is given by

$$\Lambda_D \overline{\Sigma}_X - \Lambda_F \overline{\Sigma} = 0, \tag{47}$$

resulting in an exponentially varying salinity profile. The corresponding dimensionless salt intrusion length is given by

$$\begin{aligned} \Lambda_s &= \frac{\Lambda_D}{\Lambda_F} \ln(30\overline{\Sigma}_0) \\ &= \mathrm{Fr}^{-1} \ln(30\overline{\Sigma}_0). \end{aligned} \tag{48}$$

Regime II, the Chatwin regime, is characterized by a balance between vertical shear dispersion due to gravitational circulation T_{GG} and river-induced flushing T_F. The dominant salt balance in Regime II reads

$$\Lambda_{GG}^3 \overline{\Sigma}_X^3 - \Lambda_F \overline{\Sigma} = 0. \tag{49}$$

The above balance is solved by a depth-averaged salinity profile that is proportional to $X^{3/2}$ (Chatwin 1976). The corresponding dimensionless salt intrusion length reads

$$\begin{aligned} \Lambda_s &= \frac{3\Lambda_{GG}}{2\Lambda_F^{1/3}} (\overline{\Sigma}_0^{2/3} - 0.10) \\ &\approx 0.093 \mathrm{RaFr}^{-1/3} (\overline{\Sigma}_0^{2/3} - 0.10). \end{aligned} \tag{50}$$

2) REGIME III: DOWNWIND

In the newly found down-estuary wind-driven regime, here labeled Regime III, the correlation between wind-driven estuarine circulation and wind-induced salinity shear T_{WW} forms the dominant importing process, while river-induced flushing T_F remains the main exporting process (Fig. 1). The dominant salt balance is thus given by

$$\Lambda_{WW} \overline{\Sigma}_X - \Lambda_F \overline{\Sigma} = 0. \tag{51}$$

The above equation yields an exponentially varying depth-averaged salinity profile

$$\begin{aligned} \overline{\Sigma}(X) &= \overline{\Sigma}_0 \exp\left(\frac{\Lambda_F}{\Lambda_{WW}} X\right) \\ &\approx \overline{\Sigma}_0 \exp\left(330 \frac{\mathrm{Fr}}{\mathrm{RaFw}^2} X\right), \end{aligned} \tag{52}$$

and a dimensionless salt intrusion length given by

$$\begin{aligned} \Lambda_s &= \Lambda_{WW} \Lambda_F^{-1} \ln 30 \overline{\Sigma}_0, \\ &\approx 0.0030 \mathrm{RaFw}^2 \mathrm{Fr}^{-1} \ln(30\overline{\Sigma}_0). \end{aligned} \tag{53}$$
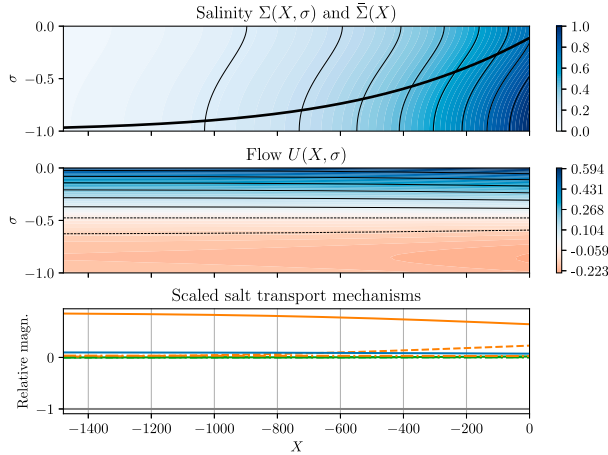
FIG. 1. An estuary in Regime III with Ra = 1000, Fr = 0.025, Fw = 1.7. (top) The dimensionless subtidal salinity profile, with depth-averaged salinity given by the solid black line. (middle) The dimensionless subtidal flow field, with red indicating up-estuary flow and blue indicating down-estuary flow. Down-estuary wind induces a circulation that enhances classical gravitational circulation. (bottom) The scaled, along-estuary transport terms that constitute Eq. (34). The plotted terms are scaled by the river transport $\Lambda_F \overline{\Sigma}$ The gray line depicts the scaled river flushing of salt T_F, which is the only exporting process in Regime III. The orange lines depict scaled T_{WW} (solid), T_{GW} (dashed), and T_{RW} (dash–dotted). The green lines depict scaled T_{GG} (solid), T_{GR} (dashed), and T_{RR} (dash–dotted). Last, the solid blue line shows the scaled dispersive transport T_D. By virtue of Eq. (34), the plotted scaled import terms add up to the riverine flushing export term.

The associated dimensional salt intrusion length reads

$$L_s \approx 0.0030 \frac{\tau_w^2 H^5 B}{Q \rho_0^2 K_M^3} \ln(30\overline{\Sigma}_0). \qquad (54)$$

Hence in Regime III, the salt intrusion is inversely proportional to the river discharge Q, and proportional to the squared wind stress τ_w^2, demonstrating a large sensitivity to wind forcing since $\tau_w^2 \sim u_a^4$ [Eq. (11)].

3) REGIME IV: UPWIND

In the newly found up-estuary wind-driven regime, here labeled Regime IV, the salt balance is dominated by a balance between the interaction of vertical shear dispersion due to gravitational circulation with up-estuary wind shear as main exporting process (T_{GW}), and the self-interaction of vertical shear dispersion due to gravitational circulation as main importing process (T_{GG}) (Fig. 2). The dominant salt transport balance reads

$$\Lambda_{GG}^3 \overline{\Sigma}_X^3 - |\Lambda_{GW}^2| \overline{\Sigma}_X^2 = 0. \qquad (55)$$

This balance results in a linear depth-averaged salinity profile:

$$\overline{\Sigma}(X) = \frac{|\Lambda_{GW}^2|}{\Lambda_{GG}^3} X + \overline{\Sigma}_0$$

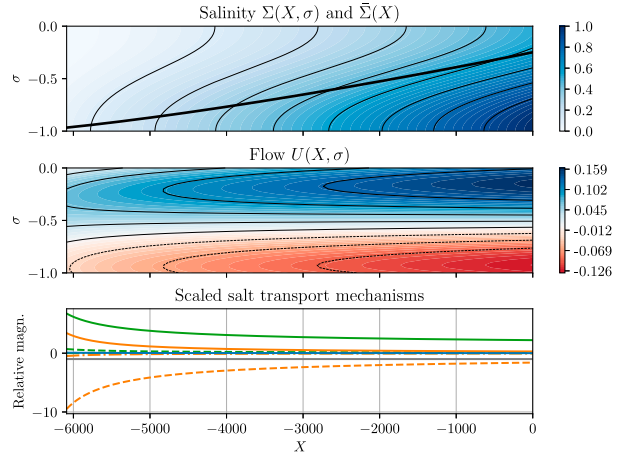$$\approx 10|Fw|Ra^{-1} X + \overline{\Sigma}_0, \qquad (56)$$

FIG. 2. An estuary in Regime IV. Here, Ra = 5×10^4, Fr = 0.025, Fw = -0.5, and the plots follow the same coloring conventions as used in Fig. 1. Note that riverine flushing T_F is dominated by T_{GW} as main exporting process throughout the estuary. The behavior at the salt intrusion limit, where the salt transport processes seem to diverge, is mostly a visual effect since the actual salinity, and therefore salt transport, is negligible there.

yielding a salt intrusion length of

$$\Lambda_s = \Lambda_{GG}^3 |\Lambda_{GW}^{-2}| (\overline{\Sigma}_0 - 1/30)$$

$$\approx 0.10 Ra |Fw|^{-1} (\overline{\Sigma}_0 - 1/30), \qquad (57)$$

which dimensionally reads

$$L_s \approx 3.0 \frac{\beta g \rho_0 H^2}{|\tau_w|} (\overline{\Sigma}_0 - 1/30). \qquad (58)$$

In Regime IV, salt intrusion is thus inversely proportional to the wind stress magnitude $|\tau_w|$ and thus inversely proportional to the square of the surface wind speed u_a^2. Additionally, the above salt intrusion length is independent of Q, K_H, and K_M.

b. Sensitivity analysis

1) REGIMES IN PARAMETER SPACE

The four salt transport regimes discussed in the previous section may be plotted in the three-dimensional parameter space, spanned by Fr, Ra, and Fw. For the sensitivity study, dimensionless numbers are varied over orders of magnitude. The Froude and estuarine Rayleigh number are varied within the same range as was done by Dijkstra and Schuttelaars (2021): $10^{-4} \leq Fr \leq 2$ and $25 \leq Ra \leq 7 \times 10^{-4}$. The dimensionless wind strain number is varied between -1 (up-estuary winds) and 8 (down-estuary winds). It will be shown that results from wind straining numbers outside this range can straightforwardly be inferred from boundary values.
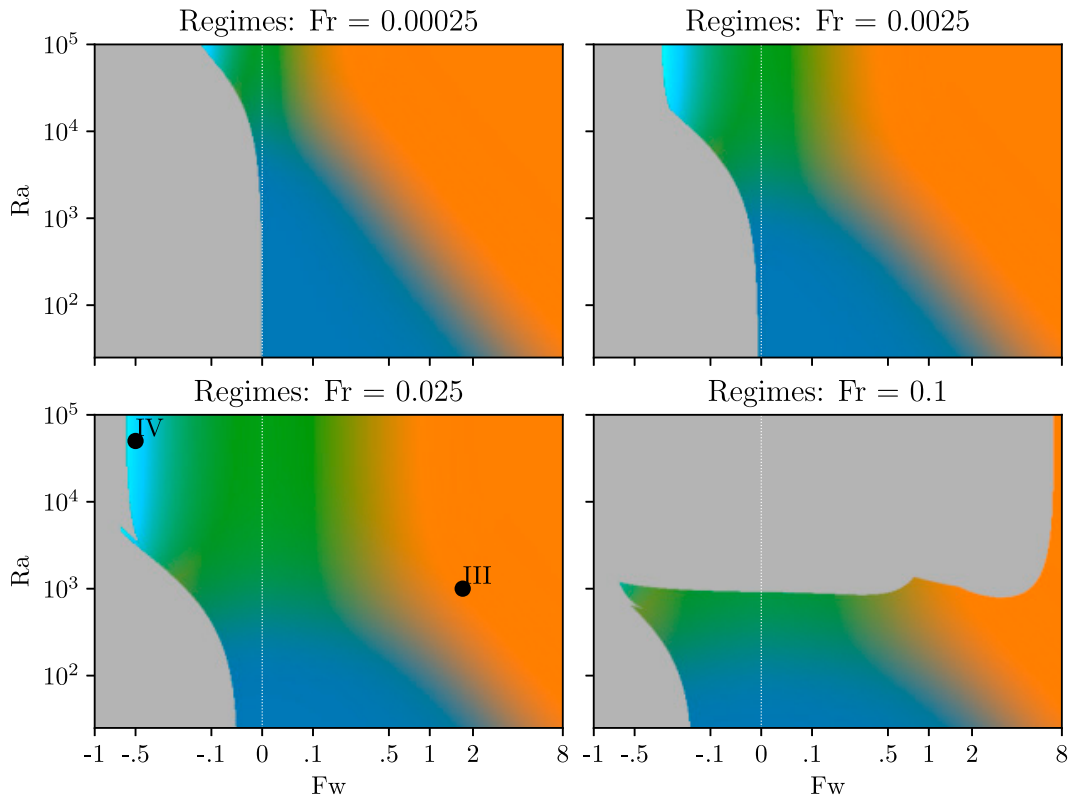
FIG. 3. Sensitivity analysis for different values of Fr. Blue denotes Regime I (dispersive), green Regime II (Chatwin), orange Regime III (downwind), and cyan Regime IV (upwind). Fw = 0 is depicted by the vertical white lines. In the lower-left panel, the locations of the parameter values of Fig. 1 (Regime III) and Fig. 2 (Regime IV) are plotted.

In Fig. 3, Fw is varied semilogarithmically, Ra is varied logarithmically, while Fr is chosen constant per plot. In all panels of Fig. 3, starting on the line Fw = 0, an increase in Ra leads to a shift from Regime I (indicated in blue) toward Regime II (indicated in green), which agrees with Dijkstra and Schuttelaars (2021). For down-estuary winds (Fw > 0), the emergence of Regime III is observed. For up-estuary winds and for large values of Ra, Regime IV is attained (except for Fr = 0.1), occupying a small region in parameter space. For small values of Ra, the gray area of model invalidity is encountered for small up-estuary wind numbers. Depending on Fr, even small up-estuary winds result in unstable stratification through up-estuary surface straining of the salinity field, which is considered to be unphysical and therefore identified as invalid in the current model. In the lower two plots of Fig. 3, regions in parameter space of solution nonuniqueness are found for certain up-estuary (negative) wind numbers and large values of Fr and Ra. In this region in parameter space, also negative salinity model realizations are encountered. All parameter regions of invalid model behavior are masked gray.

The sensitivity of model regimes to Fr may also be deduced from Fig. 3 by comparing the different panels. In general, increasing Fr pushes estuarine dynamics from Regime I or III toward Regime II. It also increases the region where solutions are well defined for up-estuary winds.

Inspection of the salinity shear in Eq. (30) indeed shows that increased Fr has a stabilizing effect on the salinity structure (much the same as increased Ra), allowing for greater up-estuary wind magnitudes. Increasing Fr even further (the bottom-right panel of Fig. 3) results in a failure to meet the model assumptions in large areas of the parameter space. This indicates that for large Fr, momentum advection cannot be neglected in the momentum equation and the salt balance may not be approximated according to Eq. (24).

2) REGIME BOUNDARIES

The boundaries between different transport regimes may be computed from the theoretical salt intrusion lengths within each regime. The demarcation of Regimes I and II is computed by equating Eq. (48) to Eq. (50), yielding

$$\mathrm{Ra} \approx 13.9 \mathrm{Fr}^{-2/3} \frac{\ln 30 \overline{\Sigma}_0}{\overline{\Sigma}_0^{2/3} - 0.10}$$

$$\sim \mathrm{Fr}^{-2/3}. \tag{59}$$

This result agrees with Dijkstra and Schuttelaars (2021). Increasing Fr or Ra will thus both push the dynamics more to the Chatwin regime (II), and Fw does not play a role in this
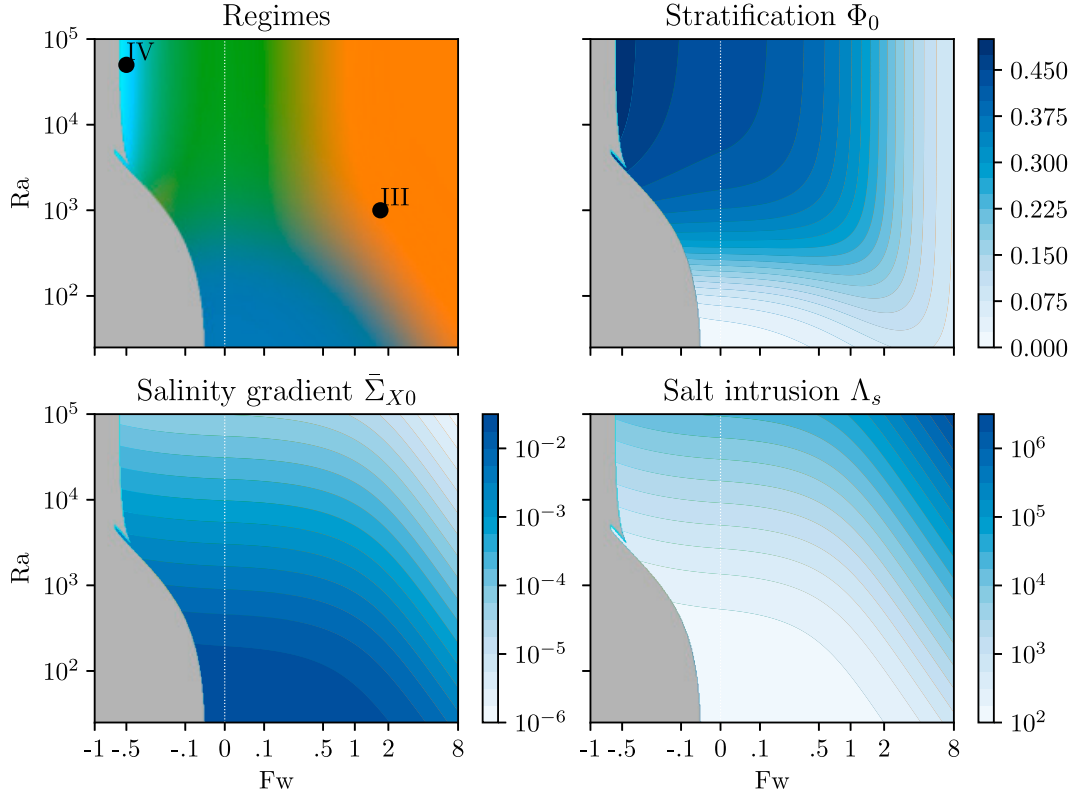
FIG. 4. Sensitivity analysis for Fr = 0.025. In the upper-left panel, the locations of the parameter values of the Fig. 1 (Regime III) and Fig. 2 (Regime IV) are plotted.

demarcation. Second, the demarcation of Regimes I and III is computed by equating Eqs. (48) and (53), yielding

$$\mathrm{Ra} \approx 330 \mathrm{Fw}^{-2}. \tag{60}$$

Systems described by lower values of Ra, being more well mixed in general, require a larger wind number to be pushed into Regime III. As the above equation indicates, this boundary is largely independent of Fr. Third, the demarcation of Regimes II and III is

$$\mathrm{Fw} \approx 4.9 \mathrm{Fr}^{1/3} \sqrt{\frac{\overline{\Sigma}_0^{2/3} - 0.10}{\ln \overline{3} 0 \Sigma_0}}$$

$$\sim \mathrm{Fr}^{1/3}. \tag{61}$$

This boundary is independent of Ra as is also demonstrated in Fig. 3. Systems described by larger Froude numbers thus require a larger wind number Fw in order to exhibit Regime III behavior. Last, Regime IV only shares boundaries with Regime II, with demarcation

$$\mathrm{Fw} \approx -1.4 \mathrm{Fr}^{1/3} \frac{\overline{\Sigma}_0 - 1/30}{\overline{\Sigma}_0^{2/3} - 0.10}$$

$$\sim -\mathrm{Fr}^{1/3}. \tag{62}$$

Additionally, the regions of model invalidity within parameter space can be computed on the basis of analytical criteria, which is done in appendix B.

3) SALT INTRUSION AND STRATIFICATION IN PARAMETER SPACE

Figure 4 shows a Fw–Ra plane in parameter space parameterized by Fr = 0.025. For clarity, the associated regime plot (Fig. 3, bottom left) is repeated as the top-left plot. The top-right panel shows the seaward stratification degree Φ_0, which ranges between 0 (no stratification) and 1 (highly stratified). The bottom-left panel shows the logarithmically scaled seaward longitudinal salinity gradient $\overline{\Sigma}_{X0}$. Last, the logarithmically scaled dimensionless salt intrusion Λ_s is plotted in the bottom-right panel.

Fw = 0 is depicted by the vertical white lines. Starting on that line, an increase in Ra is accompanied by an increase in both seaward stratification Φ_0 and salt intrusion Λ_s, and a decrease in longitudinal salinity gradient $\overline{\Sigma}_{X0}$.

For down-estuary winds (Fw > 0), we observe the emergence of Regime III. Stratification decreases monotonously when moving from Regime II toward Regime III over horizontal lines of constant Ra. However, when moving from Regime I toward Regime III, local maxima are encountered: at small values for Fw stratification increases, while for larger values of Fw when the salt balance shifts toward Regime III,

TABLE 2. Response of dimensionless salt intrusion Λ_s to Fr, Ra, and Fw for the four regimes. Symbols $\Uparrow$ and $\Downarrow$ indicate an increase and decrease in corresponding numbers or salt intrusion, respectively. Smaller arrows indicate that salt intrusion is only slightly depending on the corresponding dimensionless number, and $\times$ denotes an impossible combination.

Regime	$\Uparrow$ Fr	$\Uparrow$ Ra	$\Uparrow$ Fw > 0	$\Downarrow$ Fw < 0
I	$\Downarrow$	$\uparrow$	$\uparrow$	$\downarrow$
II	$\Downarrow$	$\Uparrow$	$\uparrow$	$\downarrow$
III	$\Downarrow$	$\Uparrow$	$\Uparrow$	$\times$
IV	$\downarrow$	$\Uparrow$	$\times$	$\Downarrow$

TABLE 3. Response of seaward stratification Φ_0 to Fr, Ra, and Fw for the four regimes. Symbols $\Uparrow$ and $\Downarrow$ indicate an increase and decrease in corresponding numbers or stratification, respectively. Smaller arrows indicate that stratification is only slightly depending on the corresponding dimensionless number, and $\times$ denotes an impossible combination.

Regime	$\Uparrow$ Fr	$\Uparrow$ Ra	$\Uparrow$ Fw > 0	$\Downarrow$ Fw < 0
I	$\Uparrow$	$\Uparrow$	$\Uparrow$	$\Downarrow$
II	$\Uparrow$	$\Uparrow$	$\Downarrow$	$\Uparrow$
III	$\Uparrow$	$\uparrow$	$\Downarrow$	$\times$
IV	$\Uparrow$	$\uparrow$	$\times$	$\Uparrow$

stratification decreases again. The longitudinal salinity gradient decreases and salt intrusion increases monotonically for increasing Fw.

For up-estuary winds (Fw < 0) and for large values of Ra, Regime IV is attained and we observe an increase in stratification, a slight increase in salinity gradient, and a slight decrease in salt intrusion moving from Regime II toward Regime IV. For small values of Ra, stratification is generally small and decreases only slightly for stronger up-estuary wind numbers. Both the salinity gradient and salt intrusion are largely unaffected by up-estuary winds when Ra is small.

Inspection of the lower two panels reveals an approximately inversely proportional relation between the seaward salinity gradient and the scaled salt intrusion length, which can be understood from linearly approximating the depth-averaged salinity at $X = 0$. Increasing Fr increases the seaward stratification Φ_0, increases the along-channel salinity gradient $\overline{\Sigma}_{X0}$ and decreases salt intrusion Λ_s, regardless of values of Ra and Fw. Consequently, Fig. 4 is indicative of the main trends of regimes, seaward stratification, longitudinal salinity gradient, and salt intrusion throughout the three-dimensional parameter space.

The previous observations can be summarized in Tables 2 and 3, which depict the response of salt intrusion and salinity stratification per regime.

Table 2 shows the response of the salt intrusion length to varying dimensionless parameters within each regime. Fr always reduces salt intrusion when increased, although within Regime IV this response is less pronounced since Fr does not appear explicitly in the asymptotic salinity structure solution. This is in contrast to Ra, which increases salt intrusion everywhere except when in Regime I. Since Ra increases when K_M or K_H decrease, when not in Regime I, increased mixing leads to decreased salt intrusion. Within Regime I, this effect is less pronounced. Down-estuary wind stress increases salt intrusion, but only has a strong influence when in Regime III. Up-estuary winds decrease salt intrusion, which is most pronounced in Regime IV. In short, the response of salt intrusion to the governing dimensionless parameters is as follows: irrespective of transport regime, the sign of the response is the same, although the magnitude of the response may vary between regimes. As for stratification, the response is less straightforward, indicated in Table 3.

Table 3 shows that increasing Fr or Ra always increases stratification, with a smaller influence of Ra on Φ_0 in the wind-driven regimes III and IV. Interesting behavior occurs when studying the influence of Fw on Φ_0. When in Regime I, stratification increases for increasing winds. However, it decreases in Regime II and continues to decrease in Regime III. For up-estuary winds, stratification increases if the dynamics take place in Regime II, attaining a maximum in Regime IV. Summarizing, as a function of Fw, Φ_0 behaves opposite, depending if the dynamics take place in Regime I or in II, III, or IV.

We may explain this different response to up-estuary than to down-estuary wind forcing depending on model regimes. Not considering wind-induced mixing, there is a competition between two mechanisms. First, surface wind stress induces salinity shear, which increases stratification for down-estuary winds and vice versa. Second, the influence of wind forcing on salt intrusion affects shear via its approximately inversely proportional relation with the seaward salinity gradient, in turn influencing stratification through gravitational effects. This mechanism acts opposite to wind straining. In Regime I, the straining mechanism is dominant, while in Regime II, III, and IV, the latter mechanism dominates. The relation between transport regime and dominant wind mechanism is indicated in Fig. 5, which serves as an exemplary summary of the results. Wind-induced mixing, the third mechanism by which wind alters the salinity structure that is considered in the present work, further adds to this picture and will be discussed in section 4.

4. Discussion

a. Effects of wind-induced mixing

Literature provides ambiguous results on the effects of wind on stratification. Besides the two mechanisms of wind influencing the salinity structure discussed so far (wind straining and wind-induced modulation of the along-channel salinity gradient), wind-induced mixing is also considered important (Scully et al. 2005; Chen and Sanford 2009). Hence, in this section, we will explore the effects of wind-induced mixing as a third mechanism by which wind influences the estuarine salinity structure. We show that we may then explain the ambiguous results in literature. To this end, we conduct experiments with several values of H and K_M in which τ_w is varied. We specifically vary dimensional parameters instead of dimensionless parameters, as this is more intuitive.
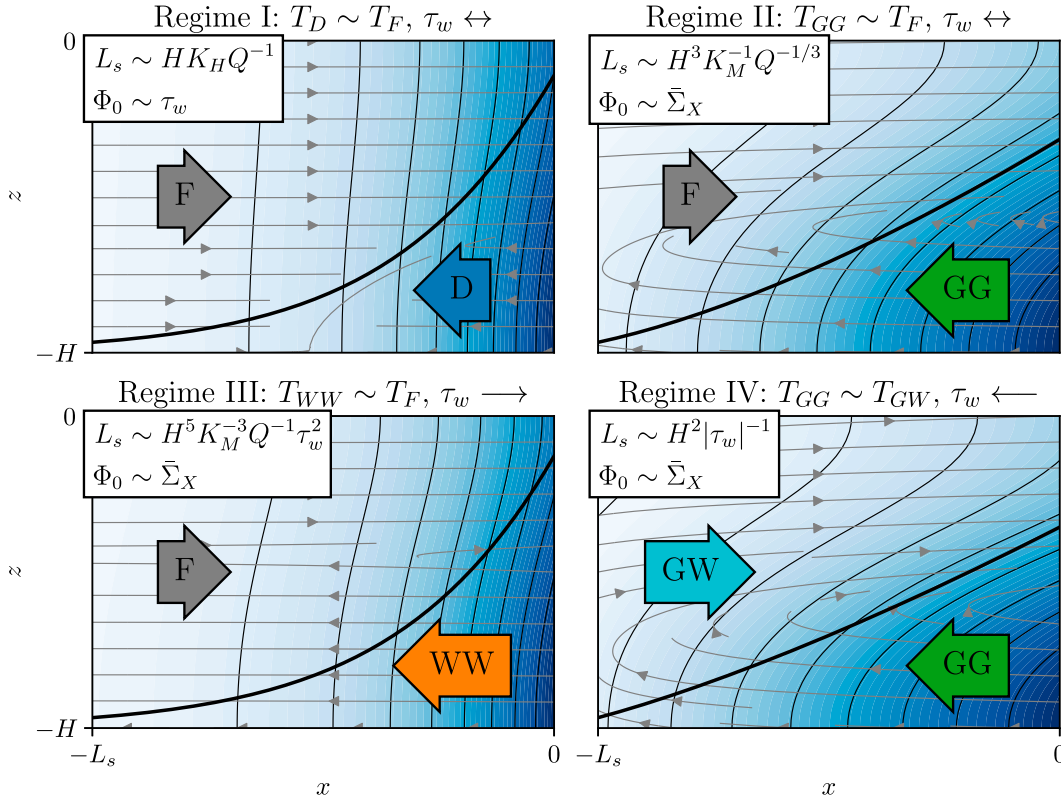
FIG. 5. A schematic overview of the four estuarine regimes proposed herein. The four regimes are shown together with their characteristic depth-averaged salinity profiles (solid black lines), spatial salinity structure (blue color and thin contour lines, where dark colors represent a higher salinity), and flow (curved streamlines). The dimensionless vertical velocity components are exaggerated to be made visible. The main importing and exporting processes are indicated by the large colored arrows, which represent the dominant balances identified in section 3a. Characteristic salt intrusion lengths per regime are also provided. Last, the dominant mechanism influencing stratification as a function of wind stress is noted per regime, with "$\sim\tau_w$" representing the straining mechanism, and "$\sim\bar{\Sigma}_X$" representing the along-channel salinity gradient mechanism.

To include the mechanism of wind-induced mixing, we employ the simple parameterization based on Kullenberg (1976):

$$K_M = K_{M0} + \omega|\tau_w|, \qquad (63)$$

where $\omega \geq 0$ (m³ s kg⁻¹, omitted in the following) is a fixed constant determining the relative influence of wind-induced mixing on the vertical eddy viscosity and diffusivity (via their dependence parameterized by Sc).

In our experiments, we compare the case without wind mixing ($\omega = 0$) to two physically realistic values of ω also discussed by Kullenberg (1976): $\omega = 4.1 \times 10^{-5}/(C_d\rho_a)$ and $\omega = 8.1 \times 10^{-5}/(C_d\rho_a)$, where $C_d = 0.0026$ and $\rho_a = 1.225$ kg m⁻³. We emphasize that the goal of this parameterization is to qualitatively visualize the influence of $K_M - \tau_w$ coupling, based on the fact that surface wind stress transfers energy to the water column, resulting in enhanced vertical mixing. Other parameterizations (e.g., a k–ϵ model) will yield different numerical values for resulting salt intrusion and stratification, but are expected to give similar trends. In Fig. 6, three

idealized estuaries of different depth are depicted, τ_w is varied and per system, and ω is also varied. It is clear that these estuaries respond differently to varying wind stress, which is explained by the different regimes the estuaries are located in.

First, we consider the model without wind-induced mixing ($\omega = 0$), depicted by the solid lines in Fig. 6. In shallow estuaries (as exemplified in the top panels), increasing τ_w leads to an increase in stratification and Regime III is attained only for very strong wind stress. Estuaries of intermediate depth (middle panels) show little response to wind forcing for small wind magnitudes, but a large decrease in stratification for progressively stronger down-estuary winds. Deep estuaries (bottom panels) typically show only a decrease in stratification for growing down-estuary winds, and an increasing stratification for up-estuary winds. Salt intrusion always increases for increasing Fw, as is also indicated in Table 2. Indeed, the response of salt intrusion to along-channel wind stress documented in previous studies, namely, that down-estuary winds increase salt intrusion and up-estuary winds decrease it (North et al. 2004; Xu et al. 2008; Uncles and Stephens 2011), is contained in Table 2.
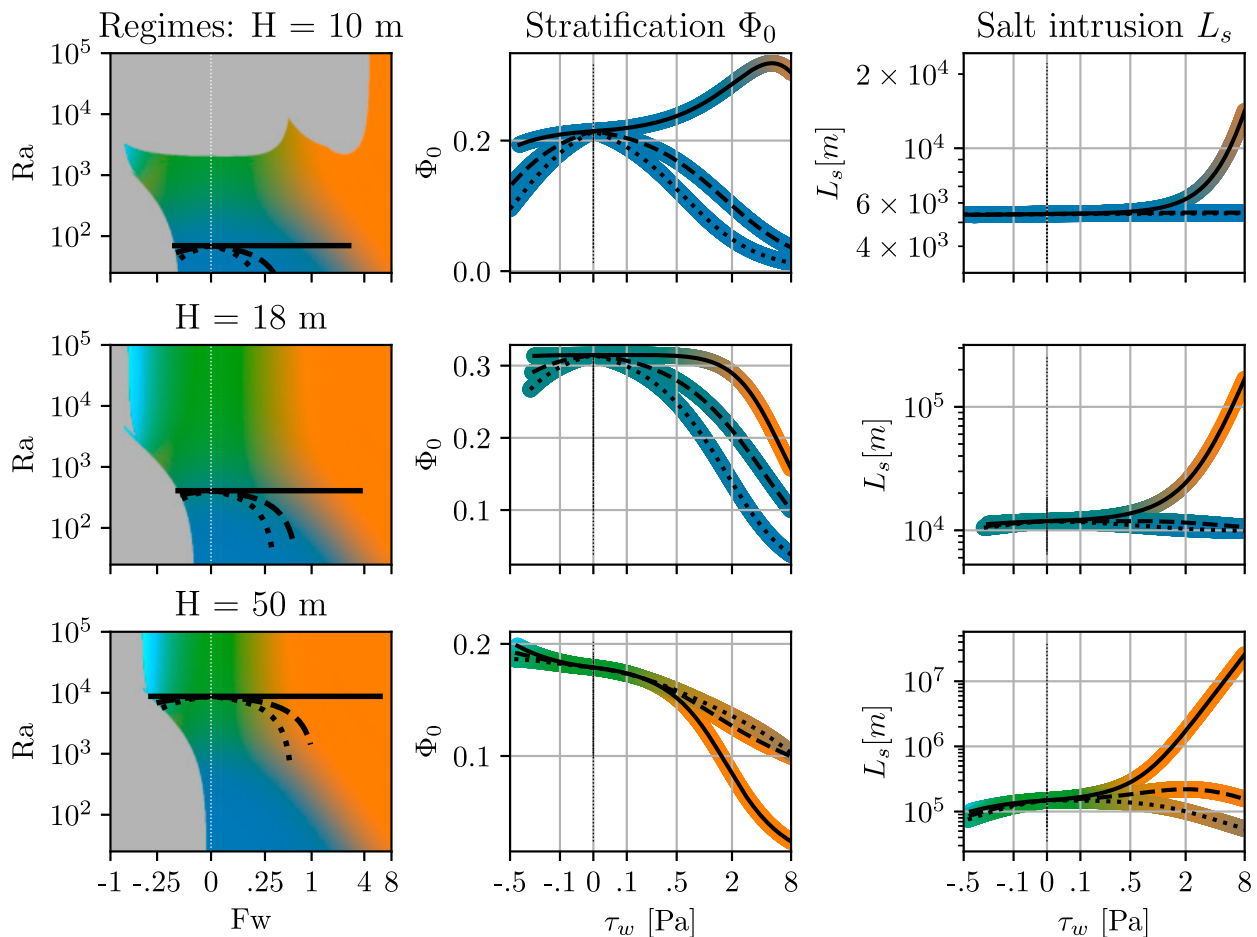
FIG. 6. Dimensional responses to axial wind forcing. Between the different systems, only the estuarine depth was varied: in the upper system, $H = 10$ m; in the middle system, $H = 18$ m; and in the lower system, $H = 50$ m. Further dimensional model parameters are $Q = 1000$ m^3 s^{-1}, $K_H = 160$ m^2 s^{-1}, and $K_M = 0.02$ m^2 s^{-1}. The wind stress τ_w is varied between different up- and down-estuary winds, with $\tau_w = 0.5$ Pa corresponding to a wind speed of $u_a = 12.5$ m s^{-1} or Beaufort number 6, and $\tau_w = 35$ Pa corresponding to a wind speed of $u_a = 33$ m s^{-1} or Beaufort number 12 [Eq. (11)]. (left) The dimensional trajectory of the sensitivity analysis through the dimensionless parameter space. (center) The seaward stratification Φ_0. (right) The dimensional salt intrusion L_s. The solid lines depict parameter trajectories without including wind-induced mixing ($\omega = 0$), the dashed and dotted lines indicate parameter trajectories following the Kullenberg (1976) parameterization, Eq. (63), with $\omega C_d \rho_a = 4.1 \times 10^{-5}$ and $\omega C_d \rho_a = 8.1 \times 10^{-5}$, respectively.

Regarding stratification, the observations by Wang (1979), Weisberg and Sturges (1976), Elliott (1978), van de Kreeke and Robaczewska (1989), North et al. (2004), Scully et al. (2005), and Xie and Li (2018), who documented an increase in stratification for down-estuary winds and a decrease for up-estuary winds, can be attributed to corresponding estuaries exhibiting Regime I behavior, depicted by the solid lines contained in the top panels of Fig. 6. In that case, salinity shear due to wind stress dominates the longitudinal salinity gradient effect of wind on stratification. For stronger winds, the latter effect starts to dominate. The response of stratification documented by Geyer (1997) and Lai et al. (2018), who observed an increase in stratification for up-estuary winds and a decrease for down-estuary winds, can be related to Regime II behavior and is seen in the lower panels of Fig. 6. This corresponds to a dominance of the longitudinal salinity gradient mechanism of wind on

stratification, over the mechanism of salinity shear due to wind stress.

Previous results on the response of stratification to wind can only partially be explained without including wind-induced mixing. To be able to explain field studies by Goodrich et al. (1987) and Stanley and Nixon (1992), who observed an overall decrease in stratification for both down- and up-estuary winds, we have to set $\omega > 0$. This corresponds to the dashed lines in Fig. 6, which are consistent with the observations by Goodrich et al. (1987) and Stanley and Nixon (1992).

Finally, the Kullenberg (1976) parameterization of vertical eddy viscosity as a function of wind stress allows for reproducing the regime diagram of Chen and Sanford (2009) in terms of the present model as follows. Their horizontal axis in Fig. 10 represents the Wedderburn number We, denotes a
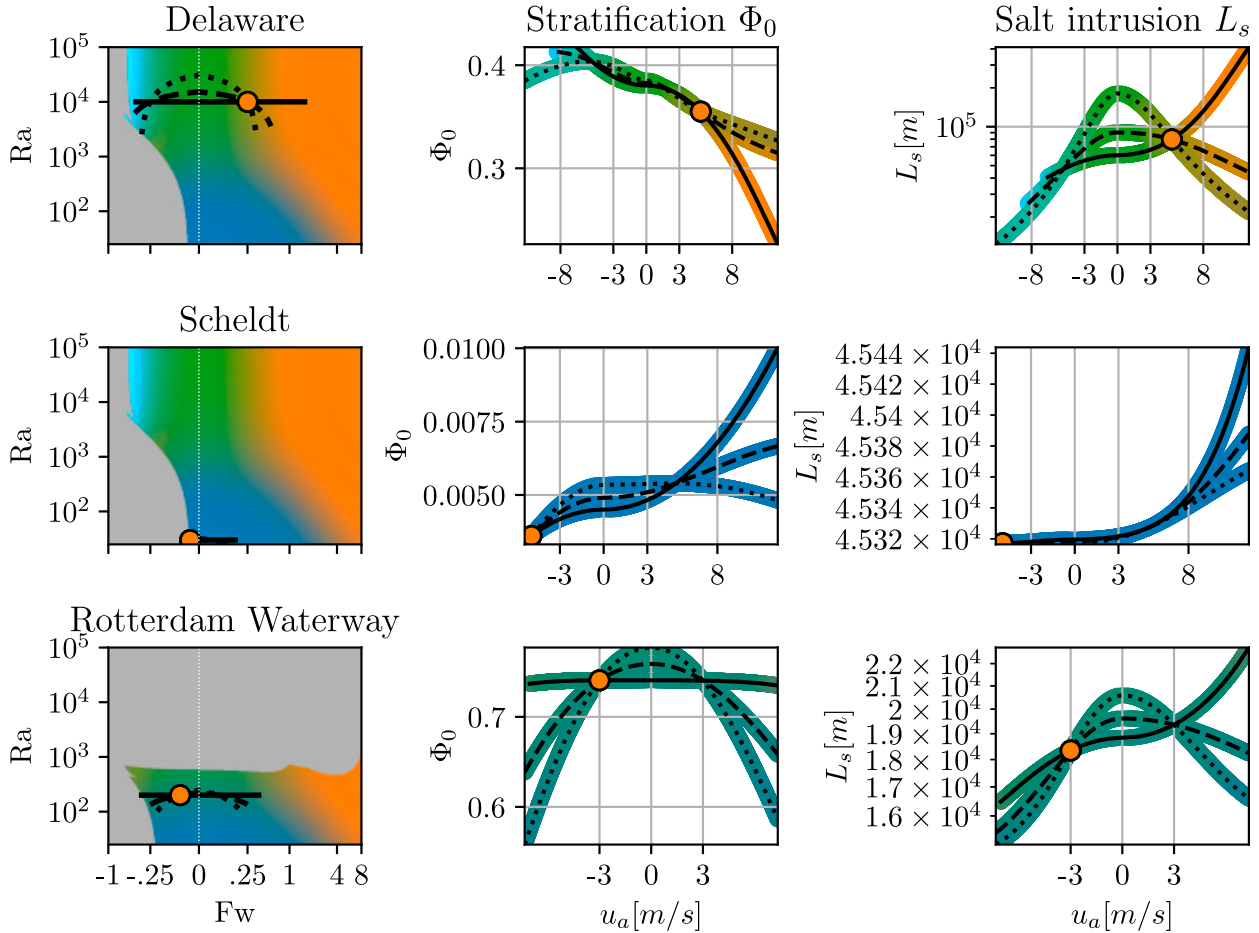
FIG. 7. Dimensional responses to axial wind forcing, with the orange dot indicating the estimated location of the estuary in parameter space. Qualitatively different behavior between the three systems can be related to different subtidal transport regimes. The values of ω are the same as in Fig. 6. The Delaware estuary is located close to the boundary between Regime II and III, whereas the Scheldt and Rotterdam Waterway estuaries are far from a wind-driven regime. Lower values of Ra reflect an estuarine robustness against wind forcing, which is also clear from the theoretical regime boundaries described in the section 3.

ratio of wind stress to along-channel baroclinic pressure gradient force. In the context of the present research, We can be viewed as We $\sim$ FwRa$^{-1}\Lambda_s$. Their vertical axis represents a fraction of the water column affected by wind-induced mixing based on an entrainment model and is proportional to $\sqrt{|\text{Fw}|}$. For down-estuary winds, the increase-then-decrease in stratification associated to a wind-induced change from Regime I to Regime III in the current work (see Table 3 and the upper panels of Fig. 6) provides an additional explanation to the explanation of Chen and Sanford (2009), namely, the competition between wind straining and wind-induced mixing. That is, modulation of the along-channel salinity gradient by wind and the corresponding change in stratification adds to the picture of Chen and Sanford (2009). For stronger winds, Fig. 10 of Chen and Sanford (2009) indicates that both down- and up-estuary winds will decrease stratification. This is consistent with our findings, but for up-estuary winds, we have to set $\omega > 0$ to account for the decrease in stratification found by Chen and Sanford (2009).

b. Application to three estuaries

To illustrate that the various regimes in the present work and corresponding different responses to wind occur in reality, we apply the model to three different estuaries: the Delaware estuary (United States, neap tide) and the Scheldt estuary and the Rotterdam Waterway (both in the Netherlands, with the latter during high discharge periods). The numbers Fr and Ra for these estuaries have been adopted from Dijkstra and Schuttelaars (2021). For the Scheldt, Fr and Ra values were adapted so that a realistic estimate of the salt intrusion length was obtained. Froude numbers of the respective estuaries are 0.02, 0.015, and 0.2, and estimated Ra numbers are 1×10^4, 30, and 200. To estimate Fw for these estuaries, typical values for τ_w, H, and K_M are required. Subtidal wind stresses have been estimated using data from the Global Wind Atlas 3.0 (DTU 2022), which provides global mean wind magnitude and direction data. Taking into account the estuarine principal axes and wind variability by weighing wind speeds using wind direction frequency roses, we estimated the

axial 10-m subtidal wind speed u_a as 5, −5, and −3 m s^{-1} for the three estuaries, respectively. Typical values for H and K_M were estimated from Aristizábal and Chant (2013), Schramkowski and de Swart (2002), and de Nijs et al. (2011) for the three estuaries, respectively. For H, we adopted typical values of 20, 10, and 15.5 m and for K_M, we chose 3×10^{-3}, 2.2×10^{-2}, and 4×10^{-3} m^2 s^{-1}. Using the quadratic wind stress law, Eq. (11), this results in a typical wind stress for the estuaries at hand, which in turn determines Fw. It is assumed that the value of Ra documented by Dijkstra and Schuttelaars (2021) was measured in the presence of the estimated subtidal wind stress, which causes the curved parameter trajectories to cross the line Fw = 0 at different values of Ra if $\omega > 0$. For our simulations, we have varied the subtidal axial wind speed on a symmetric interval around zero that includes the typical wind speed. Results are given in Fig. 7. The estuarine regime as well as typical subtidal stratification and salt intrusion agree with literature. The sensitivity of the plotted estuaries to changing subtidal wind conditions could not be verified from field experiments in literature. Starting from the top row of Fig. 7, the Delaware estuary is located on the boundary of Regime II and III and shows a large sensitivity to subtidal wind stress. This is in line with the previously derived regime boundaries: The larger Ra, the smaller Fw has to be in order to push the dynamics to wind-driven model regimes. Additionally, because of the relatively small estimated K_M for the Delaware, Fw is more sensitive to u_a, increasing the overall sensitivity of the estuarine salinity structure to subtidal wind stress. For example, a shift in wind direction would cause decreased salt intrusion on the order of tens of kilometers and would induce a regime shift. In contrast, the Scheldt estuary is insensitive to subtidal wind forcing. The Rotterdam Waterway estuary, being located on the boundary of Regime I and II, shows intermediate sensitivity to wind forcing. The effect of increasing ω also varies per estuary. Surprisingly, one cannot conclude that an increased influence of wind-induced mixing lowers stratification (upper middle panel), because the modulation of the along-channel salinity gradient in Regime III has a larger effect on decreasing stratification. However, except from Regime I, which applies to the Scheldt, a higher ω implies a decrease in salt intrusion, which agrees with theoretical derivations from section 3.

c. Model applicability and outlook

Here, we briefly discuss model limitations and resulting applicability. The model limitations are principally the result of three modeling choices visible in Fig. 7.

First, we have the choice of one parameter set per estuary. The parameters of the present model should be interpreted as typical values, parameterizing variations along indefinite dimensions in an estuary, or parts of an estuary. The present study is not intended to describe the dynamics due to longitudinal, lateral, or intratidal parameter variations. Including along-channel variations is possible when using the current model; however, then a modeled estuary can feature multiple regimes along its length, which complicates the analysis of the response to wind forcing. Our goal is to illustrate the

qualitative effect of wind on various estuaries, hence in Fig. 7, we have adopted a single set of typical parameter values representative of each estuary.

Second, the assumption of parameter uniformity through the estuarine domain deserves attention. The choice of a uniform and constant vertical eddy viscosity K_M (and thus $K_S = K_M/$Sc) restricts model applicability in cases of moderate up-estuary winds for low Ra (Fig. 7, middle-left panel). As discussed earlier, in that region, the major cause of model invalidity is unstable stratification, which is regarded unphysical on subtidal time scales. This can be mitigated by allowing K_M to vary along the estuary: K_M could be increased locally, in the region of unstable stratification, which is physically justified. A more accurate description can be obtained by varying the parameters along the estuary, or by retrieving the vertical eddy viscosity and diffusivity from a more advanced turbulence model.

Third, very large values of Fr and Ra fall outside the present model parameter domain, which can be observed in the bottom-left plot of Fig. 7. This is due to advective terms being left out of the momentum equation, and the assumption of a simplified salt balance, Eq. (24). These choices limit the model to relatively well-mixed and partially stratified conditions.

Despite these limitations, our model allows to qualitatively establish the influence of extended periods of increased wind forcing, which may trigger a regime change in the estuary. Further research is required to explore how dimensional model parameters more realistically depend on turbulence, which exerts a control on the relative importance of the competing mechanisms of wind-induced salinity shear, wind-induced modulation of the depth-averaged salinity gradient and wind-induced vertical mixing. The practical use of the current study can be appreciated from its ability to qualitatively reproduce behavior that was also found in field and complex model studies of previous authors, as discussed in the previous section, and real-life estuaries, as discussed in Fig. 7.

5. Conclusions

The salt balance of estuaries forced by river discharge, tides and wind stress has been investigated using the subtidal, width averaged model of Ralston et al. (2008). Model behavior is captured by just three dimensionless numbers: a Froude number, representing river discharge, an estuarine Rayleigh number, representing mixing, and a dimensionless wind stress number. By analyzing the three-dimensional parameter space that is generated by these numbers, four regimes were identified based on dominant salt transport balances. Regimes I and II are the tidally dispersive regime and the Chatwin regime (Dijkstra and Schuttelaars 2021). The inclusion of wind forcing induces two additional regimes: Regime III, where down-estuary wind dominates salt import, and Regime IV, where interactions involving up-estuary wind dominates salt export. We have demonstrated that salt intrusion decreases for increasing Fr and increasing up-estuary winds, and decreases for increasing Ra and down-estuary winds.

Stratification increases for increasing Fr and Ra. However, stratification only increases for down-estuary winds when in Regime I, while it decreases for up-estuary winds in that regime. It behaves oppositely if the estuary belongs to Regime II, III, or IV. In terms of physical mechanisms, the response of salt intrusion and stratification to changing subtidal surface wind stress depends on three competing mechanisms: Wind straining, wind-induced modulation of the along-channel salinity gradient and wind-induced mixing. Depending on the model regime, different mechanisms dominate the influence of wind on the estuarine salinity structure. With this, we have obtained a unified understanding of the sensitivity of salt intrusion and stratification to wind. We are able to explain ambiguous observations of previous authors regarding the behavior of stratification as function of changing wind forcing in the context of the present model. We have demonstrated that different regimes and responses to wind are likely found in different real-life estuaries. In case of an estuarine regime shift within a single estuary, which can be induced by systematic change of wind forcing, the dominant governing balance changes, causing an apparent ambiguous behavior with respect to governing parameters. Our results suggest parts of the causes of this ambiguous behavior.

Data availability statement. No datasets were generated or analyzed during the current study.

APPENDIX A

Table of Shape Functions and Constants

The shape functions $P_1, \ldots, P_6$ and the constants $C_1, \ldots, C_6$ capture the integrated cross-correlated shape functions originating from the exchange flow salinity transport term $\overline{u's'}$. The complete expressions are shown in Table A1.

APPENDIX B

Details on the Parametric Solution Method of the Depth-Averaged Salinity Equation

a. Model solution: Mathematical derivation

The differential equation governing the depth-averaged salinity is given by Eq. (35):

$$\alpha\overline{\Sigma}_X^3 + \beta\overline{\Sigma}_X^2 + \gamma\overline{\Sigma}_X - \delta\overline{\Sigma} = 0, \tag{B1}$$

with coefficients from Eq. (36). We will solve this equation by introducing a parameter r' that functions as a generalized

coordinate, such that $X = X(r')$. For the following derivation to be mathematically valid, we require $X_{r'} \neq 0$ to satisfy necessary conditions of the implicit and inverse function theorems.

First, we set $p = \overline{\Sigma}_X$ to abbreviate notation. Next, we define

$$F(X,\overline{\Sigma},p) = \alpha p^3/\delta + \beta p^2/\delta + \gamma p/\delta - \overline{\Sigma}, \tag{B2}$$

and thus, finding a root of F implies solving Eq. (B1). The method of characteristics is employed, taken from section 12.7.3 of Haberman (2013). The characteristic equations associated to the nonlinear ordinary differential equation Eq. (B1) are given by

$$p_{r'} = p, \tag{B3}$$

$$X_{r'} = \frac{1}{\delta}(3\alpha p^2 + 2\beta p + \gamma). \tag{B4}$$

Provided that $\overline{\Sigma}_{X0}$ is the unique real solution to Eq. (38) and $X_{r'} > 0$ for $r' < 0$, the above system of ordinary differential equations has a unique solution by the Picard–Lindelöf theorem. We proceed to solve for this solution. Equation (B3) is solved by a simple exponential solution $p(r') = k_1\exp(r')$. Substituting in Eq. (B4) and integrating yields the solution to the above system of equations:

$$p(r') = k_1\exp(r'), \tag{B5}$$

$$X(r') = \frac{1}{\delta}\left[\frac{3}{2}\alpha k_1^2\exp(2r') + 2\beta k_1\exp(r') + \gamma r'\right] + k_2. \tag{B6}$$

Now, since $\overline{\Sigma}_{r'} = \overline{\Sigma}_X X_{r'} = pX_{r'}$, after integration of the latter expression, the parametric solution to the depth-averaged salinity equation becomes (expressed in the generalized coordinate r')

$$\overline{\Sigma}(r') = \frac{1}{\delta}[\alpha k_1^3\exp(3r') + \beta k_1^2\exp(2r') + \gamma k_1\exp(r')] + k_3. \tag{B7}$$

Since $p = k_1\exp(r') = \overline{\Sigma}_X$, it follows from Eq. (B1) that $k_3 = 0$ immediately. It remains to solve for the constants k_1 and k_2. Let us define

$$r_0 = \{r' : X(r') = 0\}. \tag{B8}$$

Then $p(r_0) = \overline{\Sigma}_X(X = 0) = \overline{\Sigma}_{X0}$. Accordingly, $k_1 = \overline{\Sigma}_{X0}\exp(-r_0)$. By substituting $r' = r_0$ in Eq. (B6), k_2 can be expressed as

$$k_2 = -\frac{1}{\delta}\left(\frac{3}{2}\alpha + 2\beta + \gamma r_0\right). \tag{B9}$$

Substituting k_1 and k_2 in Eqs. (B5) and (B6) and defining

$$r = r' - r_0, \tag{B10}$$

such that $X(r = 0) = X(r' = r_0) = 0$, we obtain after elaboration

TABLE A1. Details on the depth-varying shape functions and cross-correlation constants.

Expression	$a \geq 0$	$a = 2$, Sc = 2.2
$P_1(\sigma)$	$\dfrac{a}{a+3}\left(\dfrac{1}{2} - \dfrac{3}{2}\sigma^2\right)$	$-\dfrac{3\sigma^2}{5} + \dfrac{1}{5}$
$P_2(\sigma)$	$-\dfrac{1}{6}\sigma^3 - \dfrac{3}{16}\dfrac{a+4}{a+3}\sigma^2 + \dfrac{1}{48}\dfrac{a+6}{a+3}$	$-\dfrac{\sigma^3}{6} - \dfrac{9\sigma^2}{40} + \dfrac{1}{30}$
$P_3(\sigma)$	$\dfrac{3}{4}\dfrac{a+2}{a+3}\sigma^2 + \sigma + \dfrac{1}{4}\dfrac{a+4}{a+3}$	$\dfrac{3\sigma^2}{5} + \sigma + \dfrac{3}{10}$
$P_4(\sigma)$	$\text{Sc}\left[\dfrac{a}{a+3}\left(-\dfrac{1}{8}\sigma^4 + \dfrac{1}{4}\sigma^2 - \dfrac{7}{120}\right)\right]$	$\text{Sc}\left(-\dfrac{\sigma^4}{20} + \dfrac{\sigma^2}{10} - \dfrac{7}{300}\right)$
$P_5(\sigma)$	$\text{Sc}\left(-\dfrac{1}{120}\sigma^5 - \dfrac{1}{64}\dfrac{a+4}{a+3}\sigma^4 + \dfrac{1}{96}\dfrac{a+6}{a+3}\sigma^2 - \dfrac{1}{2880}\dfrac{5a+36}{a+3}\right)$	$\text{Sc}\left(-\dfrac{\sigma^5}{120} - \dfrac{\sigma^4}{160} + \dfrac{\sigma^2}{60} - \dfrac{23}{7200}\right)$
$P_6(\sigma)$	$\text{Sc}\left(\dfrac{1}{16}\dfrac{a+2}{a+3}\sigma^4 + \dfrac{1}{6}\sigma^3 + \dfrac{1}{8}\dfrac{a+4}{a+3}\sigma^2 - \dfrac{1}{240}\dfrac{3a+16}{a+3}\right)$	$\text{Sc}\left(\dfrac{\sigma^4}{20} + \dfrac{\sigma^3}{6} + \dfrac{\sigma^2}{20} - \dfrac{11}{600}\right)$
$P_7(\sigma)$	$-\dfrac{1}{24}\sigma^4 - \dfrac{1}{16}\dfrac{a+4}{a+3}\sigma^3 - \dfrac{1}{48}\dfrac{5a+18}{a+3}$	$-\dfrac{\sigma^4}{24} - \dfrac{3\sigma^3}{40} - \dfrac{7}{60}$
$C_1 = -\overline{P_2 P_5}$	$\dfrac{19a^2 + 285a + 1116}{1\,451\,520a^2 + 8\,709\,120a + 13\,063\,680}\text{Sc}$	$\dfrac{881}{18\,144\,000}\text{Sc} \approx 1.1 \times 10^{-4}$
$C_2 = -2\overline{P_1 P_5}$	$\dfrac{19a^2 + 153a}{201\,60a^2 + 120\,960a + 181\,440}\text{Sc}$	$\dfrac{191}{252\,000}\text{Sc} \approx 1.7 \times 10^{-3}$
$C_3 = -2\overline{P_3 P_5}$	$\dfrac{7a^2 + 91a + 306}{40320a^2 + 241920a + 362880}\text{Sc}$	$\dfrac{43}{84000}\text{Sc} \approx 1.1 \times 10^{-3}$
$C_4 = -\overline{P_1 P_4}$	$\dfrac{2a^2}{105a^2 + 630a + 945}\text{Sc}$	$\dfrac{8}{2625}\text{Sc} \approx 6.6 \times 10^{-3}$
$C_5 = -2\overline{P_1 P_6}$	$\dfrac{5a^2 + 31a}{840a^2 + 5040a + 7560}\text{Sc}$	$\dfrac{41}{10\,500}\text{Sc} \approx 8.6 \times 10^{-3}$
$C_6 = -\overline{P_3 P_6}$	$\dfrac{a^2 + 11a + 32}{1680a^2 + 100\,80a + 15\,120}\text{Sc}$	$\dfrac{29}{21\,000}\text{Sc} \approx 3.0 \times 10^{-3}$
$C_7 = -P_4(0)$	$\dfrac{7}{120}\dfrac{a}{a+3}\text{Sc}$	$\dfrac{7}{300}\text{Sc} \approx 5.1 \times 10^{-2}$
$C_8 = -P_5(0)$	$\dfrac{1}{2880}\dfrac{5a+36}{a+3}\text{Sc}$	$\dfrac{23}{7200}\text{Sc} \approx 7.0 \times 10^{-3}$
$C_9 = -P_6(0)$	$\dfrac{1}{240}\dfrac{3a+16}{a+3}\text{Sc}$	$\dfrac{11}{600}\text{Sc} \approx 4.0 \times 10^{-2}$

$$\overline{\Sigma}(r) = \delta^{-1}(\alpha\overline{\Sigma}_{X0}^3 e^{3r} + \beta\overline{\Sigma}_{X0}^2 e^{2r} + \gamma\overline{\Sigma}_{X0}e^r), \quad (B11)$$

$$X(r) = \delta^{-1}\left[\dfrac{3}{2}\alpha\overline{\Sigma}_{X0}^2(e^{2r} - 1) + 2\beta\overline{\Sigma}_{X0}(e^r - 1) + \gamma r\right], \quad (B12)$$

$$\overline{\Sigma}_X(r) = \overline{\Sigma}_{X0}e^r, \quad (B13)$$

which are identical to Eqs. (40), (41), and (42), proving the parametric solution method.

Next, we will revisit the section on model limitations [section 2b(4)]. If possible, the regions of model (in)validity within parameter space will be quantified.

b. Boundary condition uniqueness

Let us look at the equation for the seaward salinity boundary condition (38), given by

$$\alpha\overline{\Sigma}_{X0}^3 + \beta_0\overline{\Sigma}_{X0}^2 + \gamma_0\overline{\Sigma}_{X0} - \delta = 0. \quad (B14)$$

Associated to this cubic equation, a cubic discriminant determines the number of real solutions to (77):

$$D_{30} = -18\alpha\beta_0\gamma_0\delta + 4\beta_0^3\delta + \beta_0^2\gamma_0^2 - 4\alpha\gamma_0^3 - 27\alpha^2\delta^2. \quad (B15)$$

If $D_{30} < 0$, the cubic equation has one real root and two complex conjugate roots, in which case $\overline{\Sigma}_{X0}$ is unique and real. If $D_{30} = 0$, the cubic has three real roots, of which two are multiple roots. If $D_{30} > 0$, the cubic has three real, distinct roots. Substituting definitions for the cubic coefficients, one observes that the cubic discriminant of the seaward boundary condition equation generally increases for increasing Fr, Ra and decreasing Fw, consistent with the general applicability of the present model, which is
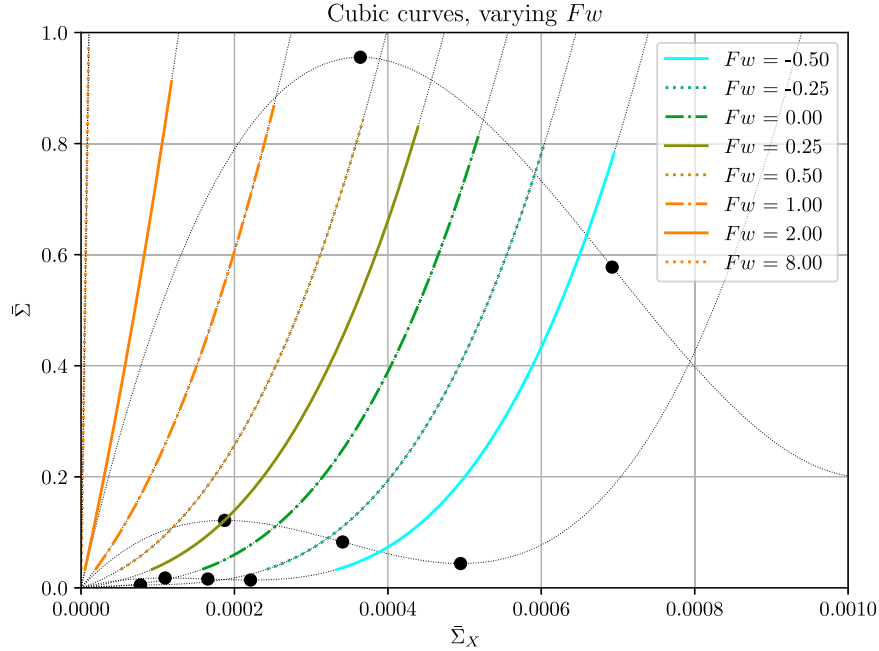
FIG. B1. Cubic curves with corresponding regime coloring for varying Fw, adopting Fr = 0.02 and Ra = 10000. A straight line indicates an exponential salinity profile (Regime III, in this case). Regimes II and IV are also visible (with Fw = 0 and Fw = −0.5, respectively). The gray curves exhibit local extrema within the model domain and corresponding parameter values are considered to be invalid. Local maxima in the Fw = −0.5 curve belonging to Regime IV are found in the region where salinity is assumed negligible, beyond the salt intrusion length, which implies that the size of Regime IV in parameter space depends on the definition of salt intrusion length.

restricted to well-mixed dynamics, roughly parameterized by low Fr and Ra.

c. Up-estuary solution existence and uniqueness

Second, a condition for uniqueness of the up-estuary model solution may be derived. Recall that for the implicit function theorem to hold, $X_r \neq 0$ for all $r \in [r_\epsilon, 0]$. Since X_r is continuous [see Eq. (B12)] and $X_r > 0$ for $r \uparrow 0$, this condition is equivalent to $X_r > 0$ for all $r \in [r_\epsilon, 0]$. Adopting notation from section a of the current appendix, this amounts to the condition

$$3\alpha p^2(r) + 2\beta p(r) + \gamma > 0, \qquad (B16)$$

for $r \in [r_\epsilon, 0]$, with $p = \overline{\Sigma}_{X0}(r)$. Since $\alpha > 0$, a sufficient condition for the above expression to hold is given by

$$D_2 = \beta^2 - 3\alpha\gamma < 0. \qquad (B17)$$

There exists another way to arrive at an equivalent conclusion, showing that the parametric solution method described here, is not more restricted than the Euler integration method of MacCready (2004). Indeed, to apply this iteration method, $\overline{\Sigma}_X$ needs to be solved from a known $\overline{\Sigma}$ iteratively. This involves solving a cubic equation at every iteration step, which only has a unique real solution if

corresponding discriminant is negative. Written out, a sufficient condition for a well-defined Euler iteration scheme is given by the discriminant of Eq. (B1):

$$D_3(\overline{\Sigma}) = -27\alpha^2\delta^2\overline{\Sigma}^2 + (4\beta^3\delta - 18\alpha\beta\gamma\delta)\overline{\Sigma} + \beta^2\gamma^2 - 4\alpha\gamma^3. \qquad (B18)$$

The Euler iterative scheme of MacCready (2004) produces a unique solution if $D_3(\overline{\Sigma}) < 0$ for all $\overline{\Sigma}$. This condition is satisfied if [again, taking the discriminant of Eq. (B18) w.r.t. $\overline{\Sigma}$]

$$(4\beta^3\delta - 18\alpha\beta\gamma\delta)^2 + 108\alpha^2\delta^2(\beta^2\gamma^2 - 4\alpha\gamma^3) < 0 \qquad (B19)$$

which is equivalent to

$$\delta^2(4\beta - 12\alpha\beta)^2(\beta^2 - 3\alpha\gamma) < 0, \qquad (B20)$$

where the last factor in the above expression is identical to D_2 [Eq. (B17)], and other factors are always positive. Finally, the criterion $D_2 < 0$ for unique up-estuary model solutions can be interpreted geometrically. Looking back at Eq. (B1), the graph $(\overline{\Sigma}_X, \overline{\Sigma})$ forms a cubic curve. Within this curve, local extrema may be found, depending on the equation coefficients. This leads to a nonunique Euler iterate at such a local extremum: For one $\overline{\Sigma}$, there exist multiple $\overline{\Sigma}_X$

values that satisfy Eq. (B1), so at such a local extremum, the next iterate is not uniquely determined. The cubic curve has local extrema if and only if $3\alpha\overline{\Sigma}_X^2 + 2\beta\overline{\Sigma}_X + \gamma = 0$ has two real roots, which is determined by the previously encountered D_2 [Eq. (B17)]. If $D_2 \geq 0$, the $\overline{\Sigma}_X - \overline{\Sigma}$ curve has an inflection point at

$$\overline{\Sigma}_X^0 = -\frac{\beta}{3\alpha} \qquad (B21)$$

and local extrema of $\overline{\Sigma}$ in the curve are located at

$$\overline{\Sigma}_X^{\pm} = \frac{-\beta \pm \sqrt{\beta^2 - 3\alpha\gamma}}{3\alpha}. \qquad (B22)$$

Substitution of the definitions of the cubic coefficients [Eq. (36)] shows that for Fw = 0, no local extrema can occur. Positive, down-estuary winds (Fw > 0) increase β and "move the curve to the left," such that no local extrema exist within the domain of relevance $\overline{\Sigma}_{X0}$. For up-estuary winds, however, the curve is translated to the right, which for some regions in parameter space causes local extrema to enter the model domain. Since the resulting model solution is nonunique, parameter values for which

$$\overline{\Sigma}_X^- \in [\overline{\Sigma}_{X0}e^{r_s}, \overline{\Sigma}_{X0}] \text{ or } \overline{\Sigma}_X^+ \in [\overline{\Sigma}_{X0}e^{r_s}, \overline{\Sigma}_{X0}], \qquad (B23)$$

are considered invalid parameter values and are marked gray in our parameter sensitivity analyses. The influence of Fw on the cubics $(\overline{\Sigma}_X, \overline{\Sigma})$ is depicted in Fig. B1.

d. Unstable stratification

As could be observed in section 3b, a large part of the parameter space in which Fw < 0 exhibits unstable stratification. Focusing only on bottom-surface stratification, the difference in salinity is given by $\Phi(X) = \Sigma(X, -1) - \Sigma(X, 0)$. Employing the model solution for the salinity distribution Eq. (30), we find for the along-channel stratification

$$\Phi(X) = \text{Ra}\overline{\Sigma}_X(X)[D_4\text{Fr} + D_5\text{Ra}\overline{\Sigma}_X(X) + D_6\text{Fw}]. \qquad (B24)$$

In the above expression, $D_i = P_i(-1) - P_i(0) > 0$ for $i = 4, 5, 6$. Since every term in the above equation has strictly positive domain except for Fw, we may estimate a condition for unstable stratification. That is, $\Phi(X) < 0$ is equivalent to

$$\text{Fw} < -\frac{1}{D_6}[D_4\text{Fr} + D_5\text{Ra}\overline{\Sigma}_X(X)]. \qquad (B25)$$

At the landward side of the estuary, the salinity gradient vanishes and we obtain a criterion for unstable stratification as a competition between river forcing and up-estuary surface straining of the salinity field:

$$\text{Fw} < -\frac{D_4}{D_6}\text{Fr}. \qquad (B26)$$

Expressed in dimensional parameters

$$\tau_w < -\frac{D_4}{D_6}\frac{QK_M\rho_0}{BH^2} = -\frac{3}{2}\frac{QK_M\rho_0}{BH^2}. \qquad (B27)$$

The above criterion indicates that increasing K_M or Q allows for stronger up-estuary winds to be described by the present model, while increasing H has a restricting effect.

e. Negative salinity

As is well known from the analysis of elliptic partial differential equations, the salinity Eq. (3) obeys a strong maximum principle. That is: s does not attain a maximum (or minimum) in the interior of the domain of computation $(-\Lambda_s, 0) \times (-H, 0)$, rather, maxima and minima of s are found on the boundary of this domain. However, by assuming the balance of Eq. (24), the maximum principle no longer applies and a positive solution for the salinity distribution is no longer guaranteed. Negative salinity solutions exist when assuming this balance but must be disregarded as nonphysical. From our simulations, negative salinity occurred mostly for large values of Fr, and always at the upper layer of the estuary that was being modeled. A condition for negative salinity is given by

$$\overline{\Sigma}(X) < \text{Ra}\overline{\Sigma}_X(X)[\text{Fr}C_7 + \text{Ra}\overline{\Sigma}_X(X)C_8 + \text{Fw}C_9]. \qquad (B28)$$

Since in particular Fr increases $\overline{\Sigma}_X$ but leaves $\overline{\Sigma}$ of the same order, the above condition is sensitive to increasing Fr. This can only be countered by assuming very low values of Ra (well-mixed dynamics).

APPENDIX C

Salt Transport Regimes: Derivations

Computing scaled transport

To understand the dominant processes constituting salt transport, we integrate the salt balance (the governing ODE) from the salt intrusion length $X = -\Lambda_s$ to the seaward side of the estuary $X = 0$. Denoting horizontally integrated transport as $\tilde{T}$, one obtains the integrals

$$\tilde{T}_{GG} = \Lambda_{GG}^3 \int_{-\Lambda_s}^0 \overline{\Sigma}_X^3(X)dX,$$

$$\tilde{T}_i = \Lambda_i^2 \int_{-\Lambda_s}^0 \overline{\Sigma}_X^2(X)dX, \quad \text{for } i \in \{GR, GW\},$$

$$\tilde{T}_j = \Lambda_j \int_{-\Lambda_s}^0 \overline{\Sigma}_X(X)dX, \quad \text{for } j \in \{RR, RW, WW\}, \qquad (C1)$$

$$\tilde{T}_F = -\Lambda_F \int_{-\Lambda_s}^0 \overline{\Sigma}(X)dX.$$

The exact solution method developed in this paper may be employed to directly evaluate the above integrals. Since $X(r)$ is

known analytically, we can integrate over the generalized coordinate r in the above equations by substitution. For example,

$$
\begin{aligned}
\tilde{T}_{GG} &= \Lambda_{GG}^3 \int_{-\Lambda_s}^0 \overline{\Sigma}_X^3(X) dX \\
&= \Lambda_{GG}^3 \int_{r_s}^0 \overline{\Sigma}_X^3(r) X_r(r) dr \\
&= \frac{\Lambda_{GG}^3}{\delta} \int_{r_s}^0 \overline{\Sigma}_{X0}^3 e^{3r} (3\alpha\overline{\Sigma}_{X0}^2 e^{2r} + 2\beta\overline{\Sigma}_{X0} e^r + \gamma) dr \\
&= \frac{\Lambda_{GG}^3 \overline{\Sigma}_{X0}^3}{\delta} \left\{ \frac{3}{5} \alpha\overline{\Sigma}_{X0}^2 [1 - \exp(5r_s)] \right. \\
&\quad \left. + \frac{1}{2} \beta\overline{\Sigma}_{X0} [1 - \exp(4r_s)] + \frac{1}{3} \gamma [1 - \exp(3r_s)] \right\}. \quad \text{(C2)}
\end{aligned}
$$

Carrying out this integration for all terms in the transport Eq. (34), one obtains eight integrated transport terms associated with the eight physical processes involved. The sum of these terms is 0 since there is no net salinity transport. Furthermore,

$$
\frac{1}{|\tilde{T}_F|} \sum_i \tilde{T}_i = 1 \quad \text{(C3)}
$$

for $i \in \{GG, GR, GW, RR, RW, WW, D\}$. The vector that is obtained, is further scaled by the river flushing term $\tilde{T}_F$ in order to bring this last exporting term to (minus) unity. By construction, the other terms then add up to unity. Consequently, the transport processes are assigned an RGB color vector $\mathbf{c}_i$, after which the total regime color of a parameter tuple (Fr, Ra, Fw) is assigned the color

$$
\mathbf{c}(Fr, Ra, Fw) = \sum_i \tilde{T}_i(Fr, Ra, Fw)\mathbf{c}_i. \quad \text{(C4)}
$$

Depending on the model location within the three-dimensional parameter space, different relative transport magnitudes arise, which are then transformed in colors following the above conventions. This procedure produces the regime diagram figures in the main text.

REFERENCES

Aristizábal, M., and R. Chant, 2013: A numerical study of salt fluxes in Delaware Bay estuary. *J. Phys. Oceanogr.*, **43**, 1572–1588, https://doi.org/10.1175/JPO-D-12-0124.1.

Burchard, H., 2009: Combined effects of wind, tide, and horizontal density gradients on stratification in estuaries and coastal seas. *J. Phys. Oceanogr.*, **39**, 2117–2136, https://doi.org/10.1175/2009JPO4142.1.

Chatwin, P. C., 1976: Some remarks on the maintenance of the salinity distribution in estuaries. *Estuarine Coastal Mar. Sci.*, **4**, 555–566, https://doi.org/10.1016/0302-3524(76)90030-X.

Chen, S.-N., and L. P. Sanford, 2009: Axial wind effects on stratification and longitudinal salt transport in an idealized, partially mixed estuary. *J. Phys. Oceanogr.*, **39**, 1905–1920, https://doi.org/10.1175/2009JPO4016.1.

de Nijs, M. A., J. D. Pietrzak, and J. C. Winterwerp, 2011: Advection of the salt wedge and evolution of the internal flow structure in the Rotterdam Waterway. *J. Phys. Oceanogr.*, **41**, 3–27, https://doi.org/10.1175/2010JPO4228.1.

Dijkstra, Y. M., and H. M. Schuttelaars, 2021: A unifying approach to subtidal salt intrusion modeling in tidal estuaries. *J. Phys. Oceanogr.*, **51**, 147–167, https://doi.org/10.1175/JPO-D-20-0006.1.

——, ——, and H. Burchard, 2017: Generation of exchange flows in estuaries by tidal and gravitational eddy viscosity-shear covariance (ESCO). *J. Geophys. Res. Oceans*, **122**, 4217–4237, https://doi.org/10.1002/2016JC012379.

DTU, 2022: Global Wind Atlas 3.0. Technical University of Denmark (DTU), accessed 15 April 2022, https://globalwindatlas.info.

Elliott, A. J., 1978: Observations of the meteorologically induced circulation in the Potomac estuary. *Estuarine Coastal Mar. Sci.*, **6**, 285–299, https://doi.org/10.1016/0302-3524(78)90017-8.

Geyer, W. R., 1997: Influence of wind on dynamics and flushing of shallow estuaries. *Estuarine Coastal Shelf Sci.*, **44**, 713–722, https://doi.org/10.1006/ecss.1996.0140.

——, and P. MacCready, 2014: The estuarine circulation. *Annu. Rev. Fluid Mech.*, **46**, 175–197, https://doi.org/10.1146/annurev-fluid-010313-141302.

Goodrich, D. M., W. C. Boicourt, P. Hamilton, and D. W. Pritchard, 1987: Wind-induced destratification in Chesapeake Bay. *J. Phys. Oceanogr.*, **17**, 2232–2240, https://doi.org/10.1175/1520-0485(1987)017<2232:WIDICB>2.0.CO;2.

Haberman, R., 2013: *Applied Partial Differential Equations with Fourier Series and Boundary Value Problems*. 5th ed., Pearson, 648 pp.

Hansen, D. V., and M. Rattray, 1965: Gravitational circulation in straits and estuaries. *J. Mar. Res.*, **23**, 104–122.

Kullenberg, G. E., 1976: On vertical mixing and the energy transfer from the wind to the water. *Tellus*, **28**, 159–165, https://doi.org/10.3402/tellusa.v28i2.10268.

Lai, W., J. Pan, and A. T. Devlin, 2018: Impact of tides and winds on estuarine circulation in the Pearl River Estuary. *Cont. Shelf Res.*, **168**, 68–82, https://doi.org/10.1016/j.csr.2018.09.004.

Lange, X., and H. Burchard, 2019: The relative importance of wind straining and gravitational forcing in driving exchange flows in tidally energetic estuaries. *J. Phys. Oceanogr.*, **49**, 723–736, https://doi.org/10.1175/JPO-D-18-0014.1.

MacCready, P., 2004: Toward a unified theory of tidally-averaged estuarine salinity structure. *Estuaries*, **27**, 561–570, https://doi.org/10.1007/BF02907644.

North, E. W., S. Y. Chao, L. P. Sanford, and R. R. Hood, 2004: The influence of wind and river pulses on an estuarine turbidity maximum: Numerical studies and field observations in Chesapeake Bay. *Estuaries*, **27**, 132–146, https://doi.org/10.1007/BF02803567.

Pritchard, D. W., 1952: Estuarine hydrography. *Advances in Geophysics*, Vol. 1, Academic Press, 243–280, https://doi.org/10.1016/S0065-2687(08)60208-3.

Ralston, D. K., W. R. Geyer, and J. A. Lerczak, 2008: Subtidal salinity and velocity in the Hudson River estuary: Observations and modeling. *J. Phys. Oceanogr.*, **38**, 753–770, https://doi.org/10.1175/2007JPO3808.1.

Schramkowski, G. P., and H. E. de Swart, 2002: Morphodynamic equilibrium in straight tidal channels: Combined effects of Coriolis force and external overtides. *J. Geophys. Res.*, **107**, 3227, https://doi.org/10.1029/2000JC000693.

Scully, M. E., C. Friedrichs, and J. Brubaker, 2005: Control of estuarine stratification and mixing by wind-induced straining of the estuarine density field. *Estuaries*, **28**, 321–326, https://doi.org/10.1007/BF02693915.

Stanley, D. W., and S. W. Nixon, 1992: Stratification and bottom-water hypoxia in the Pamlico River estuary. *Estuaries*, **15**, 270–281, https://doi.org/10.2307/1352775.

Uncles, R. J., and J. A. Stephens, 2011: The effects of wind, runoff and tides on salinity in a strongly tidal sub-estuary. *Estuaries Coasts*, **34**, 758–774, https://doi.org/10.1007/s12237-010-9365-3.

van de Kreeke, J., and K. Robaczewska, 1989: Effect of wind on the vertical circulation and stratification in the Volkerak Estuary. *Neth. J. Sea Res.*, **23**, 239–253, https://doi.org/10.1016/0077-7579(89)90045-8.

Wang, P. D., 1979: Wind-driven circulation in the Chesapeake Bay, winter 1975. *J. Phys. Oceanogr.*, **9**, 564–572, https://doi.org/10.1175/1520-0485(1979)009<0564:WDCITC>2.0.CO;2.

Weisberg, R. H., and W. Sturges, 1976: Velocity observations in the West Passage of Narragansett Bay: A partially mixed estuary. *J. Phys. Oceanogr.*, **6**, 345–354, https://doi.org/10.1175/1520-0485(1976)006<0345:VOITWP>2.0.CO;2.

Wu, J., 1969: Wind stress and surface roughness at air–sea interface. *J. Geophys. Res.*, **74**, 444–455, https://doi.org/10.1029/JB074i002p00444.

Xie, X., and M. Li, 2018: Effects of wind straining on estuarine stratification: A combined observational and modeling study. *J. Geophys. Res. Oceans*, **123**, 2363–2380, https://doi.org/10.1002/2017JC013470.

Xu, H., J. Lin, and D. Wang, 2008: Numerical study on salinity stratification in the Pamlico River Estuary. *Estuarine Coastal Shelf Sci.*, **80**, 74–84, https://doi.org/10.1016/j.ecss.2008.07.014.

Zimmerman, J. T. F., 1982: On the Lorentz linearization of a quadratically damped forced oscillator. *Phys. Lett.*, **89**, 123–124, https://doi.org/10.1016/0375-9601(82)90871-4.